ISSN 1590-8844
Vol. 06 No 01
2005

International Journal of Mechanics and Control

Honorary Editor: Guido Belforte

Editor: Andrea Manuello Bertetto

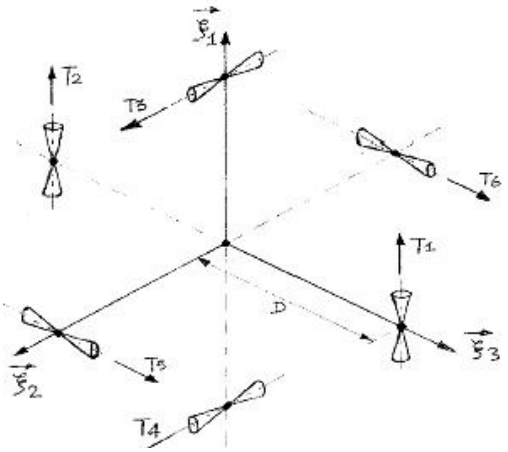

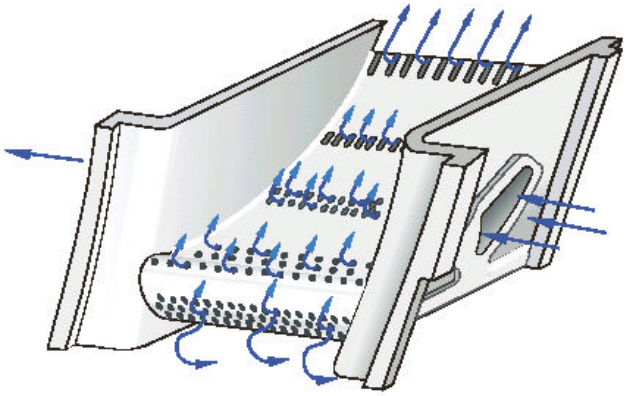

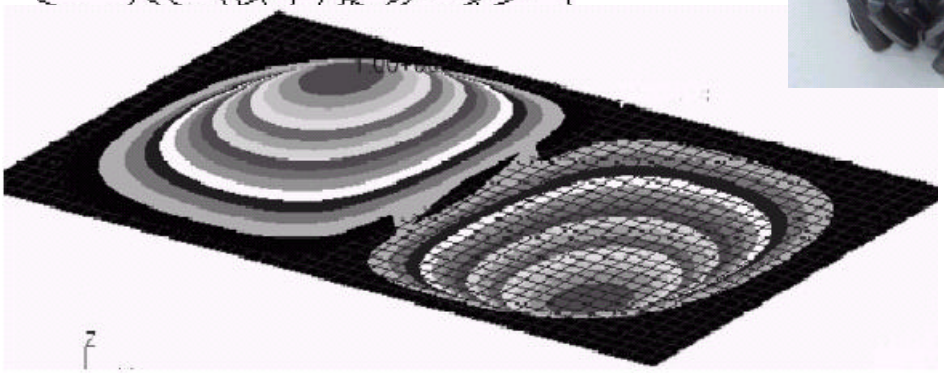

LIBRERIA EDITRICE UNIVERSITARIA
LEVROTTO & BELLA
TORINO

Editorial Board of the

International Journal of Mechanics and Control

Published by Levrotto&Bella – Torino – Italy E.C.

Honorary editor: **Guido Belforte**
Editor: **Andrea Manuello Bertetto**
General Secretariat: **Elvio Bonisoli**

Anindya Ghoshal
Arizona State University
Tempe – Arizona - USA

Domenico Appendino
Doctor Engineer
Marketing Director
Prima Industrie
Torino – Italy

Kenji Araki
Saitama University
Shimo Okubo, Urawa
Saitama – Japan

Bruno A. Boley
Columbia University,
New York - USA

Amalia Ercoli Finzi
Technical University - Politecnico di Milano
Milano – Italy

Carlo Ferraresi
Technical University - Politecnico di Torino
Torino – Italy

Nunziatino Gualtieri
Space System Group
Alenia Spazio
Torino – Italy

Giovanni Jacazio
Technical University - Politecnico di Torino
Torino – Italy

Andrea Manuello Bertetto
University of Cagliari
Cagliari – Italy

Stamos Papastergiou
Doctor
Group Leader Chief Engineer's Unit
Jet Joint Undertaking
Abingdon – United Kingdom

Mihailo Ristic
Doctor
Senior Lecturer
Imperial College
London – United Kingdom

Jànos Somlò
Technical University of Budapast
Budapest – Ungary

Jozef Suchy
Faculty of Natural Science
Banska Bystrica - Slovakia

Lubomir Uher
Institute of Control Theory and Robotics
Bratislava – Slovakia

Furio Vatta
Technical University - Politecnico di Torino
Torino – Italy

Kazuo Yamafuji
University of Electro-Communications
Tokyo – Japan

Official Torino Italy Court Registration
n.5390, 5th May 2000

Deposito presso il Tribunale di Torino
numero 5390 del 5 maggio 2000
Direttore responsabile:
Andrea Manuello Bertetto

International Journal of Mechanics and Control

Editor: **Andrea Manuello Bertetto**

Honorary editor: **Guido Belforte** ***General Secretariat:*** **Elvio Bonisoli**

The Journal is addressed to scientists and engineers who work in the fields of mechanics (mechanics, machines, systems, control, structures). It is edited in Turin (Northern Italy) by Levrotto&Bella Co., with an international board of editors. It will have not advertising.

Turin has a great and long tradition in mechanics and automation of mechanical systems. The journal would will to satisfy the needs of young research workers of having their work published on a qualified paper in a short time, and of the public need to read the results of researches as fast as possible.

Interested parties will be University Departments, Private or Public Research Centres, Innovative Industries.

Aims and scope

The *International Journal of Mechanics and Control* publishes as rapidly as possible manuscripts of high standards. It aims at providing a fast means of exchange of ideas among workers in Mechanics, at offering an effective method of bringing new results quickly to the public and at establishing an informal vehicle for the discussion of ideas that may still in the formative stages.

Language: English

International Journal of Mechanics and Control will publish both scientific and applied contributions. The scope of the journal includes theoretical and computational methods, their applications and experimental procedures used to validate the theoretical foundations. The research reported in the journal will address the issues of new formulations, solution, algorithms, computational efficiency, analytical and computational kinematics synthesis, system dynamics, structures, flexibility effects, control, optimisation, real-time simulation, reliability and durability. Fields such as vehicle dynamics, aerospace technology, robotics and mechatronics, machine dynamics, crashworthiness, biomechanics, computer graphics, or system identification are also covered by the journal.

Please address contributions to

Prof. Guido Belforte
Prof. Andrea Manuello Bertetto
PhD Dr. Eng. Elvio Bonisoli

Dept. of Mechanics
Technical University - Politecnico di Torino
C.so Duca degli Abruzzi, 24.
10129 - Torino - Italy - E.C.

e_mail: jomac@polito.it

Subscription information

Subscription order must be sent to
the publisher:

Libreria Editrice Universitaria
Leprotto&Bella
2/E via Pigafetta – 10129 Torino – Italy

www.levrotto-bella.net
e_mail: info@levrotto-bella.net
tel. +39.011.5097367
+39.011.5083690
fax +39.011.504025

ISSN 1590-8844
International Journal of Mechanics and Control, Vol. 06, No. 01, 2005

A THREE-DIMENSIONAL FINITE ELEMENT ANALYSIS OF SPUR GEARS UNDER IMPACT LOADING

Li Hongqi*, Xu Buqing*, Tong Jingwei**, Bruno Picasso***

* Shijiazhuang Railway Institute, Shijiazhuang 050043, China

** Department of Mechanics, Tianjin University, Tianjin 300072, China

*** Department of Mechanical Engineering, University of Cagliari, Italy

ABSTRACT

In this paper, the dynamic response of a spur gear under impact loading is analyzed by means of the two and three dimensional finite element method. The dynamic root stress is obtained and analysed.

Keywords: impact load, spur gear, two and three-dimensional finite element method

1 INTRODUCTION

With the development of modern industry, mechanical devices have extended their dimensional range from subminiature to large-scale units. The vibration and impact analysis of gears has been paid a great amount of attention especially in large-scale devices where gears play a critical role. A number of papers are present in the scientific literature about the application of FEM to gear stress and strain analysis since 1970. For example, Chabert [1] analysed stresses and deflection of spur gear teeth by means of two-dimensional finite element method with one tooth model. Ramamurti and Ananda Rao [2] have calculated the variations of the dynamic root stress with time by using two-dimensional finite elements and a cyclic symmetry concept. Wallace and Seireg [3] have studied the variation of dynamic stress with time under impact loading at three different points on the profile. Sahir Arilan and Kaftanoglu [4] have studied the dynamic load and root stresses in a spur gear using the concept of mesh stiffness. Vijayarangan and Ganesan [5] studied the variation of dynamic stress with time in a spur gear under a moving load and impact conditions by three-dimensional finite elements.

Contact author: Bruno Picasso

Department of Mechanical Engineering
University of Cagliari, Piazza d'Armi, 09123 Cagliari, Italy
E-mail: picasso@unica.it

2 DYNAMIC ANALYSIS OF SPUR GEARS BY MEANS OF 3D FEM

2.1 THREE-DIMENSIONAL FINITE ELEMENT MODEL

Because a three-dimensional finite model can accurately show the gear stress situation, this paper uses a whole three-dimensional finite element model to analyze the dynamic root stress of a gear under impact load. The gear is an involute spur gear.

The gear tooth parameters and the material properties are shown in Table I and Table II.

Table I Gear tooth parameters

Parameter	Value
Pressure angle	20°
Module (mm)	5
Number of teeth	20
Addendum	1 m
Dedendum	1,25 m
Face width	1,2 m
Axial circle diameter	4 m

Table II Material properties

Material	Medium Carbon Steel
Modulus of elasticity	205 GPa
Poisson ratio	0,3
Density	7800 kg/m^3

In order to obtain an high accuracy several adjacent teeth under load were discretized using a relatively dense mesh. The whole model was divided into 2034 eight node brick elements with 3450 nodes. The mesh used is shown in Fig. 1. The inner circle was fixed. An impact load was assumed to act at the tooth tip (the curve of impact load with time is shown in Figure 2). The load impulse duration was assumed to be 50 μs. The peak load value was 250 N/mm, the load direction was along the line of action. To study the decay of the dynamic response of the gear, stress calculation was carried out for 200 μs after load removal. The total time interval was 250 μs. The time interval was divided in 2500 intervals 0,1 μs each.

2.2 RESULTS AND ANALYSIS

Figure 3 shows the maximum principal stress of the front layer's node 438 with time under impact load, the maximum stress value is 194.809 MPa. Figure 4 shows the minimum principal stress at the front layer's node 430 with time, the minimum stress value is –235.347 MPa.

Figure 5 shows the maximum principal stress of the root nodes along the axial FG line when the stress value of the node 438 gets to the maximum. This plot shows that the stress distribution along an axial line is not constant although the load along an axial line is assumed to be such.

Figure 6 shows the maximum principal stress of part nodes (430, 432, 434, 436, 438) along line EF when the root stress value of node 438 gets its maximum value. Figure 7 shows the curve of the minimum principal stress of the part nodes along line EF as same as the conditions of the figure 6.

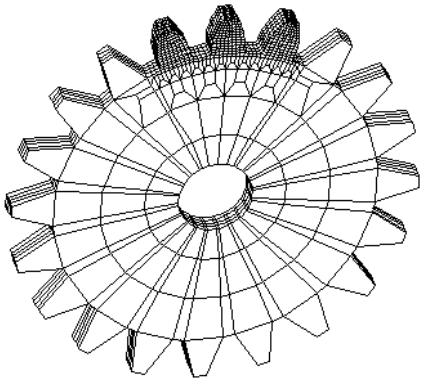

Figure1(a) FEM mesh of whole gear.

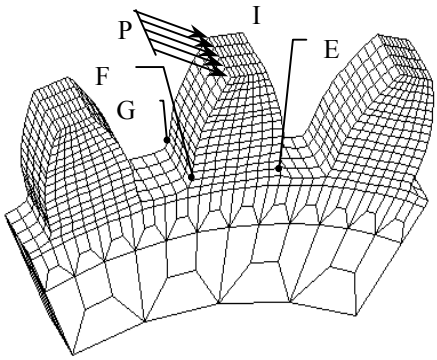

Figure 1(b). The finite element mesh of part gear.

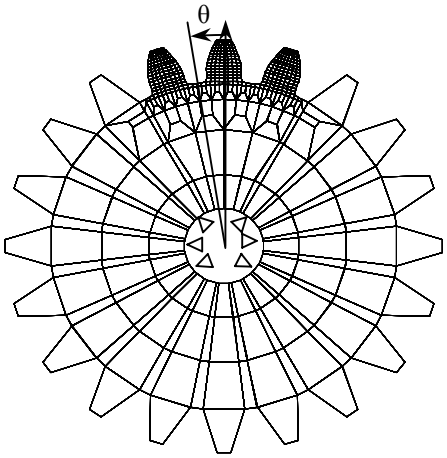

Figure1(c) Front layer view.

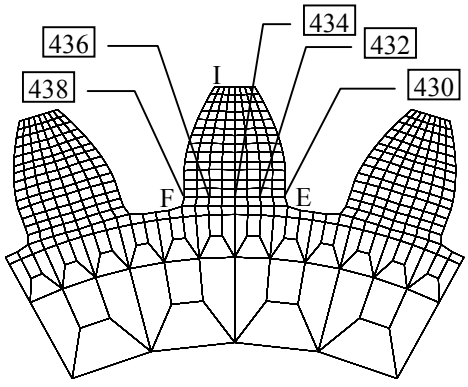

Figure 1(d) A detail of three meshed teeth.

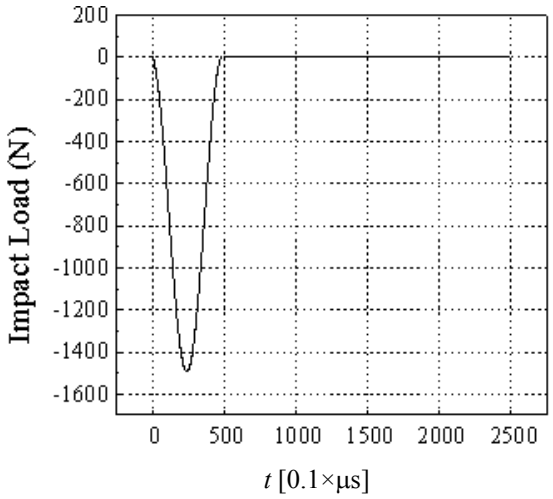

Figure 2 Impact load vs time.

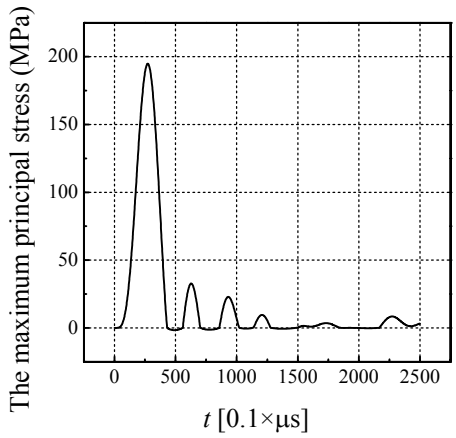

Figure 3 Maximum principal stress variation with time after impact for node 438.

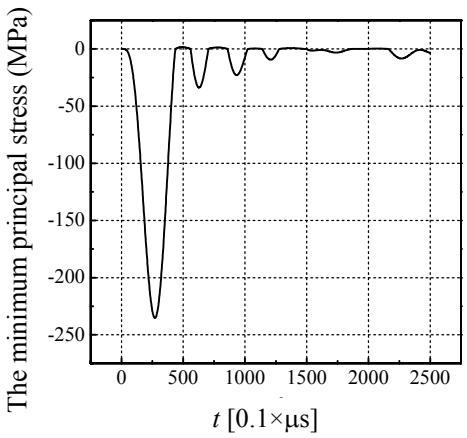

Figure 4 Minimum principal stress variation for node 430.

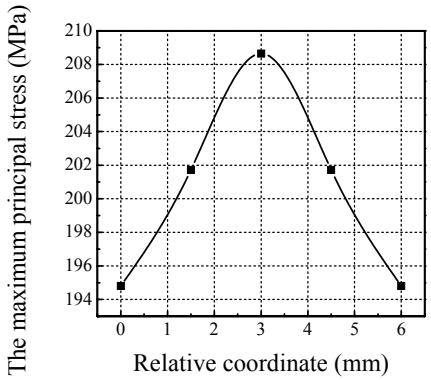

Figure 5 Max. principal stress distribution of root nodes along gear's axial direction.

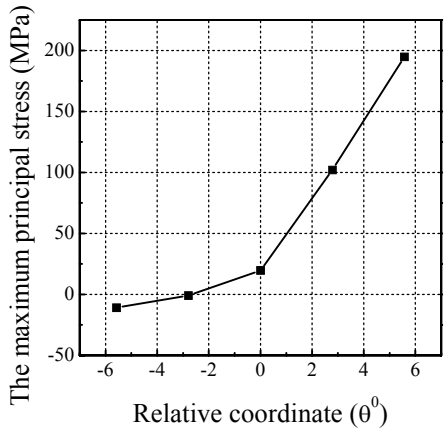

Figure 6 Maximum principal stress distributions of part nodes along line EF under impact load.

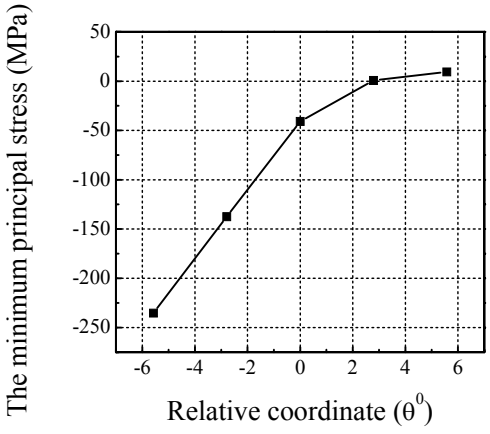

Figure 7 Minimum principal stress distributions of part nodes along line EF under impact load.

3 DYNAMIC STRESS ANALYSIS OF A SPUR GEAR UNDER IMPACT LOAD BY MEANS OF THE TWO-DIMENSIONAL FINITE ELEMENT METHOD

3.1 TWO-DIMENSIONAL FINITE ELEMENT MODEL

An additional 2-D FEM model has been developed to analyze the possibility of investigating dynamic phenomena using a cheaper and more practical model.

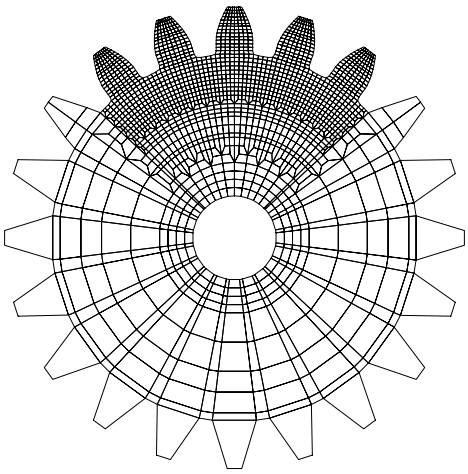

Figure 8(a) 2D Finite element mesh.

In order to obtain a good accuracy, adjacent teeth were meshed using a dense grid. The whole model was divided into 1910 four-node plane elements with 2066 nodes, 4132 degrees of freedom, as shown in Figure 8. Boundary conditions were imposed by fixing the nodes on the inner gear hole. Load location (at node 1796), value and direction were the same as those used in the three-dimensional analysis.

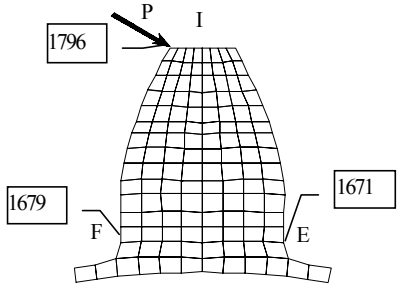

Figure 8(b) Finite element mesh of tooth I.

3.2 THE RESULTS AND ANALYSIS OF TWO-DIMENSIONAL FINITE ELEMENT MODEL

Figure 9 shows the maximum principal stresses of node 1679 with time with impacting load conditions, the maximum stress value is 208.4 MPa. Figure 10 shows the minimum principal stresses of node 1671 with time, the minimum stress value is 250.4 MPa.

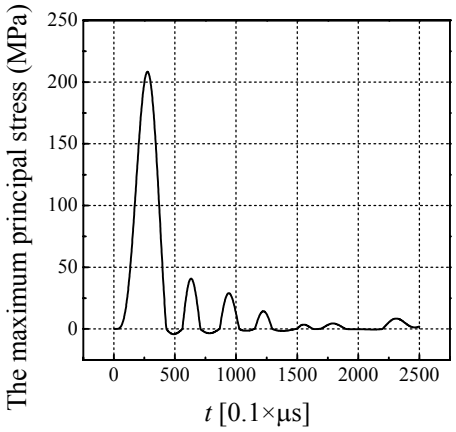

Figure 9 Maximum principal stress at node 1679.

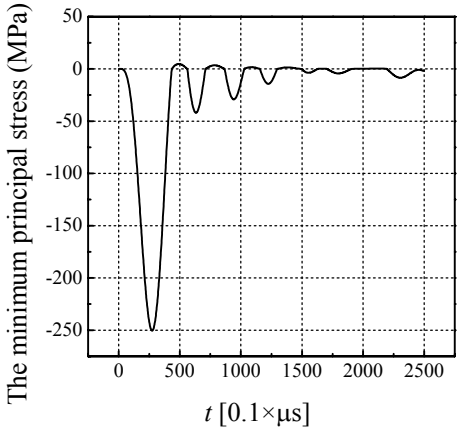

Figure 10 Minimum principal stress at node 1671 vs time.

Figure 11 shows the maximum principal stress of part nodes (1671, 1673, 1675, 1677, 1679) along line EF when the root stress value of node 1679 is maximum. Figure 12 shows the curve of the minimum principal stress of the part nodes along line EF in the same as conditions of the figure 11.

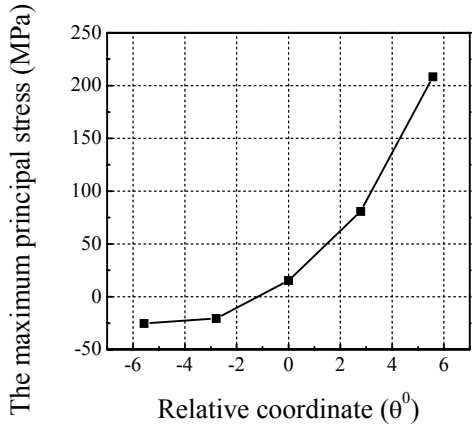

Figure 11 Maximum principal stress distribution.

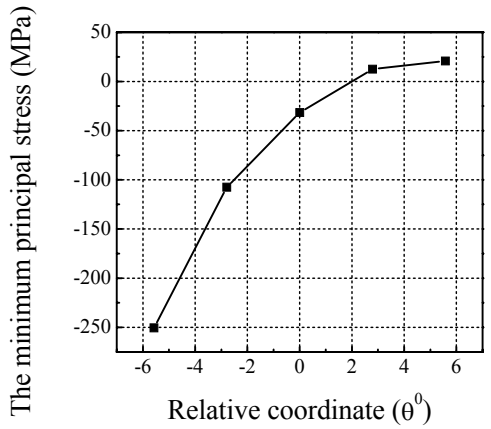

Figure 12 Minimum principal stress distribution.

4 CONCLUSIONS

1. Comparison with 3-D finite elements: The maximum principal stress (at 1679 node) and the minimum principal stress (at 1671 node) of 2-D finite element analysis are respectively higher 6.52% and 6.01% than those of 3-D finite element analysis.
2. The results of three-dimensional finite method greatly reflect the axial stress distribution.

REFERENCES

[1] Chabert G., Tran T.D., Mathis R., An evaluation of stresses and deflection of spur gear teeth under strain, *ASME Journal of Engineering for Industry*, 96, 85-93, 1974.

[2] Ramamurti V. and Ananda Rao M., Dynamic analysis of spur gear teeth. *Computers and Structures*, Vol. 29, No. 5, pp. 832-843, 1988.

[3] Wallace D.B. and Seireg A., Computer simulation of dynamic stress, deformation, and fracture of gear teeth, *ASME Journal of Engineering for Industry*, 95, 1108-1114, 1973.

[4] Sahir Arilan M.A. and Kaftanoglu B., Dynamic load and root stress analysis of spur gear. *Annals of the CIRP*, Vol. 38, No. 1, pp. 171-174, 1989.

[5] Vijayarangan S. and Ganesan N., A study of dynamic stresses in a spur gear under a moving line load and impact load conditions by a three-dimensional finite element method. *Journal of Sound and Vibration*, Vol. 162, No. 1, pp. 185-189, 1993.

ISSN 1590-8844
International Journal of Mechanics and Control, Vol. 06, No. 01, 2005

LASER HOLE DRILLING

Domenico Appendino

Prima Industrie S.p.A.

ABSTRACT

Laser drilling is achieved by focusing the Nd:YAG laser beam onto the component at sufficient intensity to melt and vaporise the material which is being drilled. It has many benefits as opposed to other processes such as high incidence angles, the ability to produce shaped holes and the higher substantial rates. These methods are described in the following article in a simple and understandable manner.

Keywords: Nd:YAG lasers

1 INTRODUCTION

Nd:YAG lasers are an important tool in today's advanced manufacturing industry.
Hole drilling is an area where Nd:YAG lasers are used extensively. The laser is capable of producing good quality, high aspect ratio holes, in a variety of materials, at very high speeds.
The benefits of laser hole drilling have made it attractive to both the aerospace and power generation industries where they have been widely adopted in the production of jet engine and gas turbine components. Probably the most common application of laser drilling is the production of small holes 0.3-0.8 mm dia. in critically heated parts such as nozzle guide vanes, blades and combustor liners. Many thousands of holes are introduced in the surface of these components to allow a film of cooling air to flow over the component.
Film cooling both extends the life of the component and enables extra performance to be achieved from the engine.
In the past, the production of these holes was achieved almost exclusively using Electro Discharge Machining (EDM). Although EDM is capable of producing good quality holes it is substantially slower than the laser and is not suited to the production of holes at high or variable incidence angles where multi-wire heads cannot be used. It also requires relatively complex consumable tooling and electrolyte fluids, both of which contribute adversely to the cost of hole production.

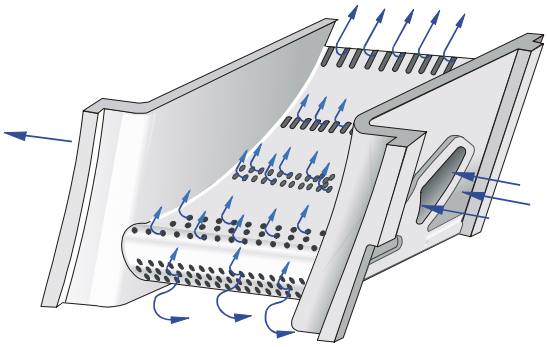

Figure 1 Aero-engine component showing film cooling flow

EDM is also not suitable for drilling through ceramic or ceramic coated materials.

2 LASER DRILLING

The process of laser drilling requires that the laser beam is focused onto the component at sufficient intensity to cause the material to melt and vaporise (boil). To achieve vaporisation temperatures within the short duration (1 or 2milli-seconds) of a laser pulse requires laser intensities in excess of $1x10^7$ W/cm^2 (10 megawatts per cm^2). This is achieved by focusing the beam through normal optical lenses.

Contact author: Domenico Appendino

Prima Industrie S.p.A.
Via Antonelli, 32
10097 Collegno (TO)
Italy

To make an approximate calculation of laser intensity divide the pulse peak power by the area of the focused spot. It is also necessary, both as an aid to the drilling process and as protection against expelled material, to provide a stream of assist gas, usually oxygen or air, coaxially with the laser beam through a nozzle.
Two laser drilling techniques are commonly used; percussion drilling and trepan drilling.
Percussion drilling is a method used to generate a hole with a stationary laser beam. The beam is focused at the point where a hole is to be produced and the shutter opened. A single pulse or a series of pulses remove the material in the beam path, with assistance from the gas, until a hole is formed.

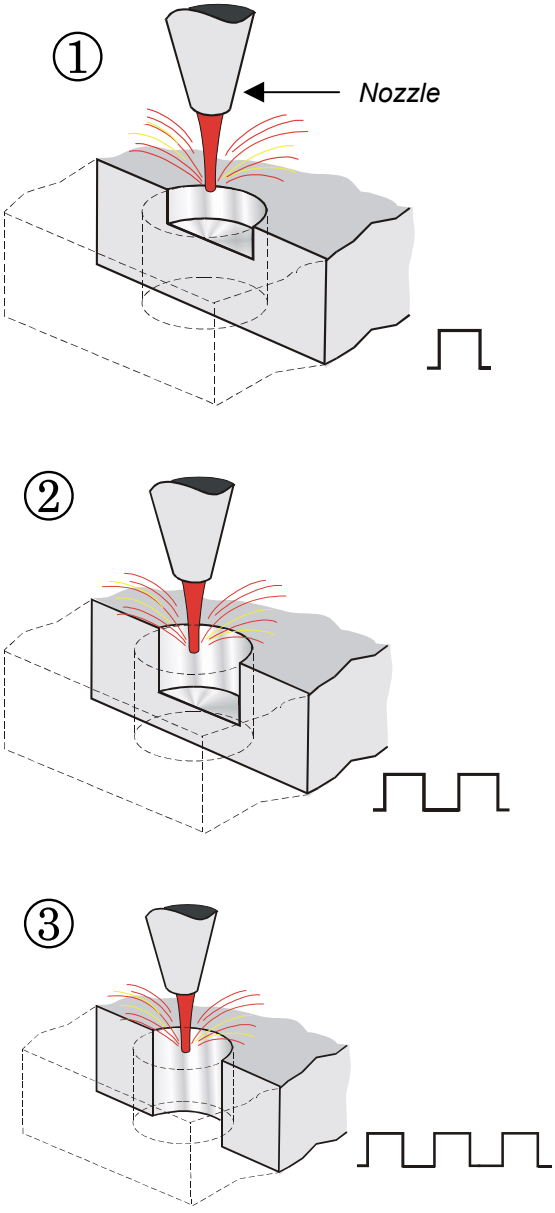

Figure 2 Percussion Drilling. Hole generated by stationary pulsed laser beam

The inherent round shape of the laser beam generates a round hole through the work piece with the hole diameter determined by the laser spot size.
Trepan drilling is a similar method except it does not rely on the laser beam size to give the final dimensions of the finished hole. Firstly, a hole smaller than intended is percussion drilled through the component (piercing). Once through, positioning equipment is used to transcribe the laser beam through an orbit describing a circular (or other shaped) path which creates the final dimensions of the hole.

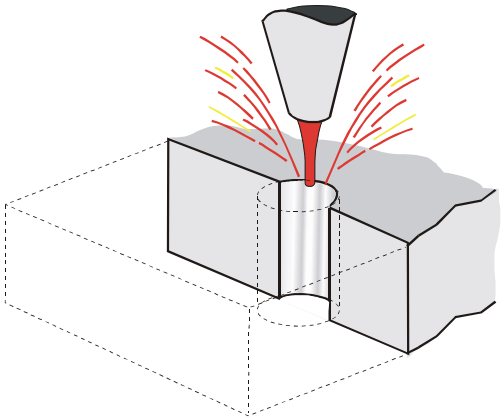

Figure 3 Trepan Drilling. Initial piercing by Percussion Drilling

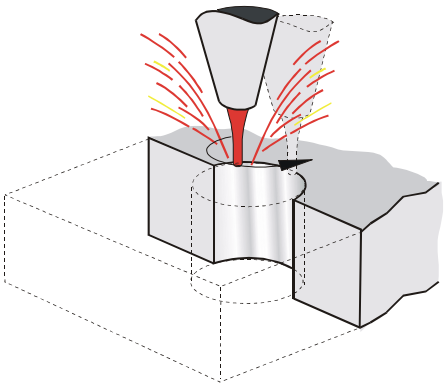

Figure 4 Trepan Drilling. Final hole sizing by moving laser around the circumference hole

Depending on the final quality requirements of the hole the beam may be required to make more than one orbit. In general trepanning gives better hole quality compared to percussion drilling although percussion drilling has the potential for faster drilling times.
An important variant of the trepanning process is the production of shaped holes. The ability to produce shaped holes allows better airflow and gives the engine designer even more scope for improving engine performance. By careful selection of parameters and detailed programming of manipulation equipment, various shapes can be generated including reverse taper and fan shaped contours.

3 DRILLING LASERS

Pulsed Nd:YAG drilling lasers have been specially developed for high quality, medium to high volume drilling applications.
The Nd:YAG drilling laser has certain features which have been tailored to enhance its drilling capability such as additional peak power, high mean power and excellent beam quality.
Enhanced peak power enables the beam intensity to be optimised for maximum material removal. As a general rule, the higher the peak power the greater the potential drilling speed and drilling depth. However, caution should be observed with this assumption, as it is important to balance the peak power used with the specific requirements of the application. The highest peak power attainable is not necessarily the one giving the best results as excessive peak power can result in unacceptable hole quality.
Beam quality is an indicator of how small the laser beam can be focused. This is an important consideration for a number of reasons. Firstly, the smaller the spot the higher the intensity that can be achieved (remember our calculation for intensity above) and therefore the more readily vaporised the material. Secondly, the focused spot size needs to be smaller than the hole that is to be drilled, very small holes require an even smaller spot size. To produce a 0.5 mm diameter hole requires a focused spot diameter between 0.2-0.4 mm. Good beam quality also enables the use of longer focal length lenses giving greater drilling depth capability and better access to complex parts.
Generally Nd:YAG drilling lasers are designed with a choice of user configurable beam quality options to allow beam quality to be selected to meet specific needs.
High mean power is a feature which has significant importance in achieving high drilling speeds. Mean power is a direct measure of the number of pulses, of particular energy, that a laser can deliver per second. If we consider that for each laser pulse a small amount of material is removed from the hole. If we are able to deliver a lot of pulses in a short time, as with a high mean power, the faster the material removal rate, the greater the drilling speed and the shorter the drilling cycle time.
The characteristics of the laser pulse can also have significant bearing on the laser's ability to drill holes. Pulse shaping is the term used to describe the tailoring of the pulse characteristics for improved hole quality and increased drilling speed. The lasers ability to allow pulse shaping is therefore desirable.

4 MATERIALS

Most metallic materials are suitable for laser drilling including the common engineering materials such as steel, stainless steel, and alloy steels.
In jet engines and gas turbines the creep and oxidation resistant nickel-chrome based 'super alloys' are also suitable for high quality laser drilling.
Nd:YAG Lasers are also suited to drilling through ceramic materials and heat resistant coatings, which are applied to the surface of some critical engine components.

5 HOLE QUALITY

For a particular application there may be very strict quality requirements for drilled holes.
In considering laser hole drilling it is useful to be aware of some of the quality factors of importance. The quality standards for hole drilling set in the aerospace industry are probably some of the most stringent in the world. The laser is perfectly capable of producing holes to these very high standards.

Some important quality features to be aware of are:

- hole diameter,
- roundness,

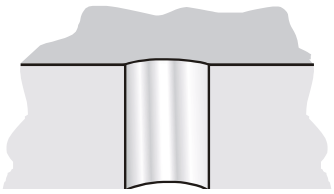

Figure 5 Normal hole

- taper,

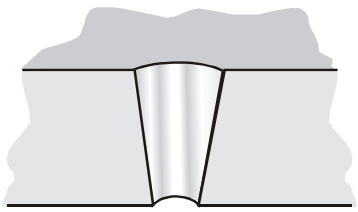

Figure 6 Taper

- bell-mouthing,

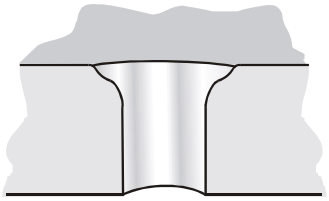

Figure 7 Bell-mouthing

- barrelling,

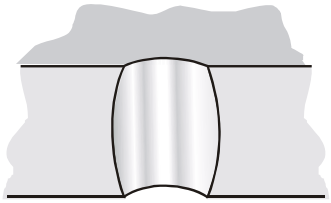

Figure 8 Barrelling

- recast layer thickness,
- cracking.

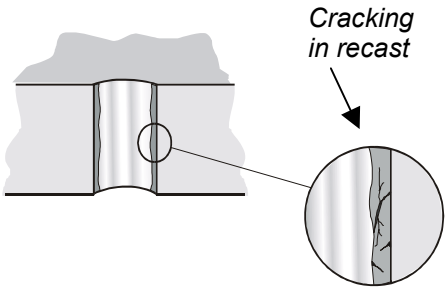

Figure 9 Location of recast laser

Of primary concern to the component designer is achieving adequate airflow through the holes so that the appropriate cooling is provided. Airflow is governed principally by the size and shape of the hole and hence the need for tight control of size, roundness and taper. There are other factors also to consider; holes are often very closely positioned to one another on a component and any deviation in size may adversely encroach on other holes or may even weaken the component locally. Excessive bell -mouthing or barrelling is therefore undesirable.
The thermal nature of the laser process does result in some melting within the hole. This can often be seen under microscopic inspection of the hole cross-section as a thin re-solidified or recast layer. Quality requirements often dictate a maximum thickness of this layer and that it should be firmly attached within the hole.
Cracking may or may not occur within the recast or parent material.
It is often the case that very small cracks can be tolerated but larger cracks and cracks that extend into the parent material may be unacceptable.

6 MACHINE CONSIDERATIONS

Industrial components requiring laser drilled holes, such as aero-engine parts, fall into two main categories, complex three-dimensional castings (nozzle guide vanes and blades) and relatively thin gauge fabricated sheet metal three-dimensional parts (combustor liners, metering panels). To laser drill holes in these type of components requires the machine or positioning system to deliver a focussed beam accurately and to a repeatable position on the surface of the component. This can be achieved by moving the beam, the component, or a combination of both of these. It is usual to integrate the drilling laser with a purpose built 5+ axes machine tool. It is important to keep the beam path length constant (fixed length) as this then maintains the same spot diameter independent of where the hole is positioned on the component and the system will drill the same size hole. This is normally achieved by moving the comparatively lightweight laser head around in at least one axis. The machine should have a seamless interface to the laser, and take complete control of all laser functions. Automatic focus control, crash protection, quick recovery, easy on-line teaching and interface to off-line programming all need to be considered. It is important to recognise that hole drilling cycle times are a combination of drilling time and machine positioning time. High speed, high quality laser drilled holes are achieved by a combination of laser and machine and these need to be considered in tandem and not isolation.

7 IN SUMMARY

Laser drilling offers very significant benefits over other processes, the main ones being higher production rates, leading to a substantially lower cost (compared to EDM), the ability to drill holes at high incidence angles (15-20 degs to the component surface) and also the ability to produce shaped holes.

REFERENCES

[1] Baxter R., Turbine Drilling. *Industrial Laser Solutions*, February, 2002.

[2] Brezonick M., Cutting Edge Application of Advanced Laser Machining. *Diesel & Gas Turbine Worldwide*, October, 2002.

ISSN 1590-8844
International Journal of Mechanics and Control, Vol. 06, No. 01, 2005

BUCKLING AND POSTBUCKLING BEHAVIOUR OF ANISOTROPIC RECTANGULAR PANELS UNDER LINEARLY VARYING COMBINED LOADS

Giacomo Frulla

Department of Aerospace Eng., Politecnico di Torino

ABSTRACT

An analytical solution has been obtained with regard to the buckling and post-buckling of anisotropic rectangular panels subjected to several combinations of uniform shear and linearly varying biaxial in-plane loads. The principle of stationary value of the total potential energy in conjunction with the Galerkin procedure was used to determine the non linear solution to the post-buckling behaviour of symmetric laminates. Different boundary conditions were considered in the analysis. The analytical results are in good agreement with the results available in the literature. They are largely influenced by transverse compressive load and boundary conditions along the four edges. A numerical FE analysis was also carried out in order to simulate the analytical behaviour of the panel. Results show satisfactory correlation.

Keywords: buckling and post-buckling analysis, anisotropic panels, linearly varying combined loads

1 NOMENCLATURE

A_{ij} - D_{ij} = extension and bending stiffness matrices,
a, b = plate dimensions in x and y directions, respectively,
E_1 ,E_2 ,G_{12}=Young's and in-plane shear moduli of the lamina,
M, N = number of terms in the series for w,
M_x, M_y = moments per unit length,
N_x, N_y, N_{xy} = force per unit length ,
N_{xcr}, N_{ycr}= buckling load per unit length, in x and y directions respectively,
w = out-of-plane deflection,
X_m , Y_n = characteristic functions for w,
$?_y$, $?_x$ = linear coefficients defining the distribution of in-plane loads ,
di, e_i = numerical constants defining the clamped-clamped beam functions,
$?$, = (x/a) not-dimensional longitudinal coordinate,
$?$ = (y/b) not-dimensional transverse coordinate,
$?_{12}$ = Poisson's ratio of the lamina.

Contact author: Giacomo Frulla

Dept. of Aerospace Eng., Politecnico di Torino,
Corso Duca degli Abruzzi 24 – 10129 Torino, Italy
Phone +39.011.5646842 Fax:+39.011.5646899

2 INTRODUCTION

Many analytical and experimental results are available in the literature on buckling and post-buckling behaviour of composite panels. Most of the results published concern uniform in-plane loads applied along the edges [1]. In most cases the experimental results concern uniaxial compression or shear loads only; in very few reports results have been reported for combination of biaxial compression and shear load applied simultaneously [2]. However a linearly varying load applied along the panel edges has to be taken into consideration in the design of various aerospace structure elements: box-beam webs, for example, are subjected to combined in-plane bending, transverse compression (due to crushing loads), and uniform shear; fuselage panels or launch vehicle structures are subjected to combined non-uniform loads. Some research has been carried out in the past on isotropic plates under these loading conditions ([4], [5]). Recently the buckling behaviour of anisotropic rectangular plates under linearly varying combined loads has been investigated [3]. A good correspondence was pointed out between the numerical-analytical results and experimental results. By the use of the Rayleigh-Ritz method Rao [6] evaluated the buckling behaviour of fibre-reinforced plastic rectangular sandwich panels with all edges simply supported, under the combined action of biaxial

compression in-plane bending and shear. Nemeth ([7], [8]) presented an exhaustive parametric study of the buckling behaviour of infinitely long anisotropic plates. The same R.R. method was used to obtain the numerous generic buckling-design charts, applicable to a broad class of infinitely long laminate panels. However the trigonometric functions used to satisfy the clamped boundary conditions along the two long edges are not particularly suited to shorter rectangular panels. The linearly varying combined loads configuration has been taken into consideration in the present analysis of the buckling and post-buckling behaviour of anisotropic rectangular panels with a symmetric layout. The buckling behaviour was mainly studied in [3] and it is introduced here as a starting point for the post-buckling investigation. Different boundary conditions have been considered: the simply supported one, the clamped one and their combinations. The stationary value of the total potential energy in conjunction with the Airy function has been used in order to have a two unknowns-two equations problem. A nonlinear algebraic approximate system has been obtained by means of the Galerkin method. The computer program POBUCK [9] has been modified in order to include such loading conditions and obtain the post-buckling configuration of the panel. A comparison with the numerical investigations performed by FEM code has been reported. A satisfactory correlation has been detected.

3 THEORETICAL ANALYSIS

The analysis is an update of previous derivations. For this reason the analytical back-ground is only summarized, while referring to the cited reports for a more detailed description. For many engineering applications, the plate in-plane dimensions-to-thickness ratio is greater than 35. In such cases, transverse shear deformation does not significantly affect the laminate behaviour. Within the hypothesis of the classical lamination theory, by introducing the nonlinear strain-displacement relations and the usual constitutive relations, it is possible to obtain the subsequent non linear governing system ([9], [10]):

$$\begin{aligned} &N_{x,x} + N_{xy,y} = 0 \\ &N_{y,y} + N_{xy,x} = 0 \\ &M_{x,xx} + 2M_{xy,xy} + M_{y,yy} + N_x w_{,xx} + N_y w_{,yy} + 2N_{xy} w_{,xy} + \\ &+ N_x w_{0,xx} + N_y w_{0,yy} + 2N_{xy} w_{0,xy} = 0 \end{aligned} \tag{1}$$

The introduction of the Airy function reduces it as follows:

$$\begin{aligned} &D_{11} w_{,xxxx} + 4D_{16} w_{,xxxy} + 2(D_{12} + 2D_{66}) w_{,xxyy} + 4D_{26} w_{,xyyy} + D_{22} w_{,yyyy} + \\ &- \left(\psi_{,yy} w_{,xx} + \psi_{,xx} w_{,yy} - 2\psi_{,xy} w_{,xy} + \psi_{,yy} w_{0,xx} + \psi_{,xx} w_{0,yy} - 2\psi_{,xy} w_{0,xy}\right) = 0 \end{aligned} \tag{2}$$

$$\begin{aligned} &A_{11}^* \psi_{,yyyy} - 2A_{16}^* \psi_{,xyyy} + \left(2A_{12}^* + A_{66}^*\right) \psi_{,xxyy} - 2A_{26}^* \psi_{,xxxy} + A_{22}^* \psi_{,xxxx} = \\ &= \left(w_{,xy}^2 - w_{,xx} w_{,yy} + 2w_{0,xy} w_{,xy} - w_{0,yy} w_{,xx} - w_{0,xx} w_{,yy}\right) = 0 \end{aligned} \tag{3}$$

with the inclusion of the compatibility equation in order to have a two equations-two unknowns problem. Specific attention is posed on the boundary condition in order to fulfil the theoretical ones by trial functions of the solution method. Specific integrals have to be included into the Galerkin transformation as the boundary condition are not completely satisfied. The out-of-plane deflection has been expressed by the following series in the case of clamped boundary condition:

$$w = \sum_m^M \sum_n^N C_{mn} X_m(x) Y_n(h) \tag{4}$$

with:

$$Z_i(z) = \cosh(\varepsilon_i z) - \cos(\varepsilon_i z) - d_i \left[senh(\varepsilon_i z) - \sin(\varepsilon_i z) \right] \tag{5}$$

where: $Z=X,Y$; $i=m,n$; and $\xi=\xi,\eta$ respectively. The constant ε_i , d_i , have been determined with high precision (16 digits) to verify the following properties : $Z_i(0) = Z_i(1) = Z_{i,\xi}(0) = Z_{i,\xi}(1) = 0$. A simple double trigonometric series is considered when simply supported condition is under analysis. The introduction of the right boundary conditions and the initial imperfection allow the transformation of the governing system into an algebraic nonlinear system by means of the Galerkin procedure. A compacted form of the system is as follows:

$$\sum_{mn} C_{mn} D_{mn}^{ij} = \sum_{pq} C_{pq} K_{pq}^{ij} + \sum_{pqrs} C_{pq} F_{rs} G_{pqrs}^{ij} + T\left(K0^{ij} + \sum_{rs} F_{rs} G0_{rs}^{ij} \right) \tag{6}$$

$$\sum_{mn} F_{mn} A_{mn}^{ij} = \sum_{pqrs} C_{pq} C_{rs} B_{pqrs}^{ij} + T\left(\sum_{pq} C_{pq} B0_{pq}^{ij} \right) \tag{7}$$

where the C_{mn} and F_{pq} are the coefficient of the approximate expression of the transverse displacement w [9] and the approximate expression of the load respectively. The other coefficient are the matrices containing the Galerkin coefficients while T is the amplitude of the simple sinusoidal initial imperfection and the matrices with an ended zero are connected to imperfection terms [9]. The initial imperfection is not included into the new version of the program at this preliminary stage of activity. It will be considered in further development. The assumed load distribution is modified in order to include the linear variation along the panel edges for longitudinal and transverse loads. According to [3], two loading parameters are considered: ξ_y for variation along the y edge and ξ_x for variation along the x edge. The applied load distribution is as follows:

$$\begin{cases} N_x = N_{x0}\left[1 - \xi_y \dfrac{y}{b}\right] \\ N_y = N_{y0}\left[1 - \xi_x \dfrac{x}{a}\right] \end{cases} \tag{8}$$

N_{x0}, N_{y0},are conventionally the bottom loads for each edge. For uniform load $\eta=0$, for trapezoidal load $\eta=0.5$, for triangular load $\eta=1$ and for in-plane bending load $\eta=2$. The POBUCK ([9], [10]) computer program has been modified in

order to introduce the linearly varying loading in-plane condition. The set of nonlinear equations is solved using an iterative procedure according to [2]. The buckling conditions can be determined by reducing the solving system to its linear approximation. See [9] and [10], for more details. A comparison with results obtained by other procedures is indicated in the following section. FE results for the same conditions are also presented.

4 ANALYTICAL AND NUMERICAL COMPARISON

Several analytical tests have been carried out to compare these results with the ones found in the literature. An anisotropic rectangular flat panel 880x580mm is analysed under different loads and boundaries. The panel is a multilayered T800-5208 CFRP, with the following lamina properties:
$E_1=168.7GPa, E_2=8.5GPa, G_{12}=5.9GPa, ?_{12}=0.335$. It has a symmetric lay-up as $[45_2/90_5/-45_2/0_2/90_2]_{2S}$. The indicated dimensions are the usable dimensions considered in the computation. Buckling conditions have been determined under different boundary and loading combination. A series of 6x6 terms is considered sufficient for the approximation in the POBUCK results. Good correlation with [3] is obtained as indicated in Table I. A numerical finite element analysis has also been performed on this subject. 1334 QUAD4 shell elements have been introduced in the model . This has been considered sufficient for this situation. A very good correlation with the analytical results is shown in the different cases reported. Buckling modes are compared in figures 1 to 6 for the clamped-clamped case (CC). Biaxial, triangular and in-plane bending loading conditions are reported. FE results are shown in figure 1, 2 and 3. POBUCK analytical mid-plane longitudinal sections are plotted in figure 4, 5 and 6. The ratio between the in-plane unit transverse load at the bottom of the panel with the longitudinal one is indicated in each figure. The two half-wave buckling shape in the biaxial case is changed into the three half-wave one of the in-plane bending due to the different distribution of the transverse load. The half wave corresponding to the reducing transverse load becomes lower with respect to the other. A change into a different shape occurs in the in-plane bending case. A good correspondence between numerical and analytical results is shown. Several post-buckling calculations are also performed on the same panel. Typical post-buckling shapes are determined according to the specific conditions and they are used as starting point in the nonlinear solution scheme. As an example the in-plane bending case with clamped boundary is reported. The post-buckling maximum load deflection curve and the longitudinal mid-plane section deformation are plotted in figure 7 and figure 8 respectively. Both analytical and numerical results point out quite good agreement. Other cases behave in a similar way and therefore they are not repeated. Experimental buckling loads, obtained from [3], are compared to the analytical ones obtained here. They are referred to a clamped boundary condition rectangular flat panel with the same mechanical properties previously indicated. The comparisons described in Table II, show a good agreement between previous calculations and experimental results. A subsequent experimental post-buckling activity is under definition in order to check the analytical results described in this paper.

5 CONCLUDING REMARKS

An analytical post-buckling solution was obtained for anisotropic rectangular panels with various boundary conditions subjected to linearly variable edge loads. The buckling and post-buckling behaviour of such a configuration was determined and reported. The buckling results were compared to the few ones found in the literature, while the post-buckling results were compared to numerical FE ones. A good correspondence was determined when a representative model was considered. Lots of the obtained results show how the buckling and post-buckling are largely influenced by transverse compression loads and by the boundary conditions along the four edges. The post-buckling shapes are correspondent to the theoretical ones expected, while transverse displacements confirm their sensitivity to the same parameters. It is important to note that numerical and analytical expectations are in good agreement confirming the well behaved theoretical analysis. Experimental activity is under preparation in order to investigate the post-buckling behaviour in such loading conditions.

REFERENCES

[1] Whitney J.M., *Structural analysis of laminated anisotropic plates*. Technomic, Basel, 1987.

[2] Romeo G. and Frulla G., Nonlinear analysis of anisotropic plates with initial imperfections and various boundary conditions subjected to combined biaxial compression and shear loads. *International Journal of Solids and Structures*, Vol. 31, No. 6, 1994, pp. 763-783.

[3] Romeo G. and Ferrero G., Analytical/experimental behavior of anisotropic rectangular panels under linearly varying combined loads. *AIAA Journal*, Vol. 39, No. 5, 2001, pp. 932-941.

[4] Grossman N., Elastic stability of simply supported flat rectangular plates under critical combinations of transverse compression and longitudinal bending. *Journal of the Aeronautical Sciences*, Vol. 16, No. 5, 1949, pp. 272-276.

[5] Noel R.G., Elastic stability of simply supported flat rectangular plates under critical combinations of longitudinal bending, longitudinal compression and

lateral compression. *Journal of the Aeronautical Sciences*, Vol. 19, No. 12, 1952, pp. 829-834.

[6] Rao K.M., Buckling coefficients for fiber-reinforced plastic-faced sandwich plates under combined loading. *AIAA Journal*, Vol. 25, No. 5, 1987, pp. 733-739.

[7] Nemeth M.P., Buckling behavior of long anisotropic plates subjected to combined loads. *NASA TP-3568*, Nov. 1995.

[8] Nemeth M.P., Buckling behavior of long symmetrically laminated plates subjected to shear and linearly varying axial edge loads. *NASA TP-3659*, July 1997.

[9] Romeo G. and Frulla G., Experimental behavior of graphite epoxy panels with cut-outs under biaxial tension, compression and shear loads. *21st Congress of the International Council of the Aeronautical Sciences*, ICAS paper 98-4,4,2, Sept. 1998.

[10] Romeo G. and Frulla G., Postbuckling behavior of graphite/epoxy stiffned panels with initial imperfections subjected to eccentric biaxial compression loading. *International Journal of Non-Linear Mechanics*, Vol. 32, No. 6, 1997, pp. 1017-1033.

Table I Analytical and FEM longitudinal buckling load P_x (kN) with $?_y=0$

Applied load		EMASTER5	POBUCK(6x6)	NASTRAN
$N_{x0}/N_{x0};\ N_{y0}/N_{x0}$	γ_x	$S-S$	$S-S$	$S-S$
$-1/0$	0	-108.9	-109.3	-108.9
$-1/-0.6$	0	-71.9	-72.0	-71.9
$-1/-1$	0.5	-62	-62.2	-62.1
$-1/-1$	1	-72.5	-72.7	-72.5
$-1/-1$	2	-88.5	-88.8	-88.4
$N_{x0}/N_{x0};\ N_{y0}/N_{x0}$	γ_x	$C-C$	$C-C$	$C-C$
$-1/0$	0	-222.4	-222.9	-222.2
$-1/-0.6$	0	-177.9	-177.9	-177.8
$-1/-1$	0.5	-166.3	-166.4	-166.2
$-1/-1$	1	-180.2	-180.3	-180.1
$-1/-1$	2	-205.8	-206.3	-205.9
$N_{x0}/N_{x0};\ N_{y0}/N_{x0}$	γ_x	$C-S$	$C-S$	$C-S$
$-1/0$	0	-194.6	-194.7	-193.9
$-1/-0.6$	0	-163.8	-163.9	-163.3
$-1/-1$	0.5	-150.0	-150.2	-149.8
$-1/-1$	1	-157.3	-157.5	-157.1
$-1/-1$	2	-170.3	-170.6	-169.9

ISSN 1590-8844
International Journal of Mechanics and Control, Vol. 06, No. 01, 2005

Table II Analytical/Experimental and FEM Buckling load P_x (kN) with $?_y=0$

Applied load		POBUCK(6x6)	Experimental	FEM
$N_{x0}/N_{x0}; N_{y0}/N_{x0}$	γ_x	$C-C$	$C-C$	$C-C$
$-1/-0.6$	0	-177.9	-187.8	-172.7
$-1/-1$	0.5	-166.4	-160.1	-159.7
$-1/-1$	1	-180.3	-191.8	-174.1
$-1/-1$	2	-206.3	-196.5	-198.7

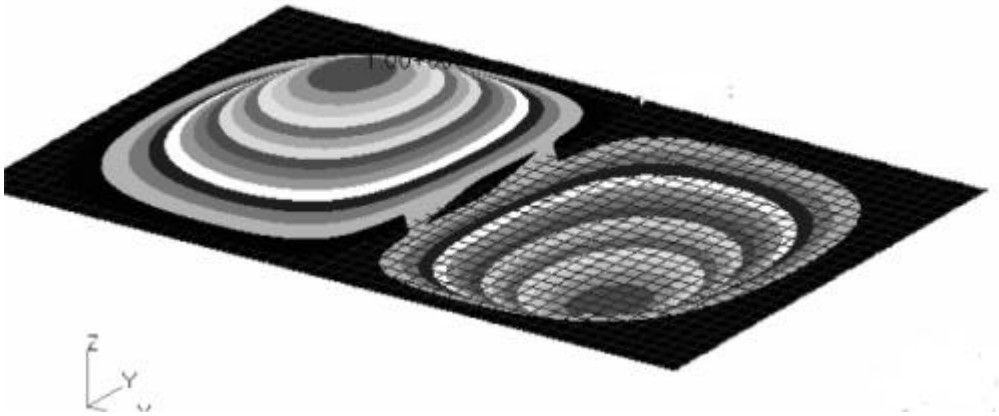

Figure 1 Uniform biaxial load (-1/-0.6/0) – CC.

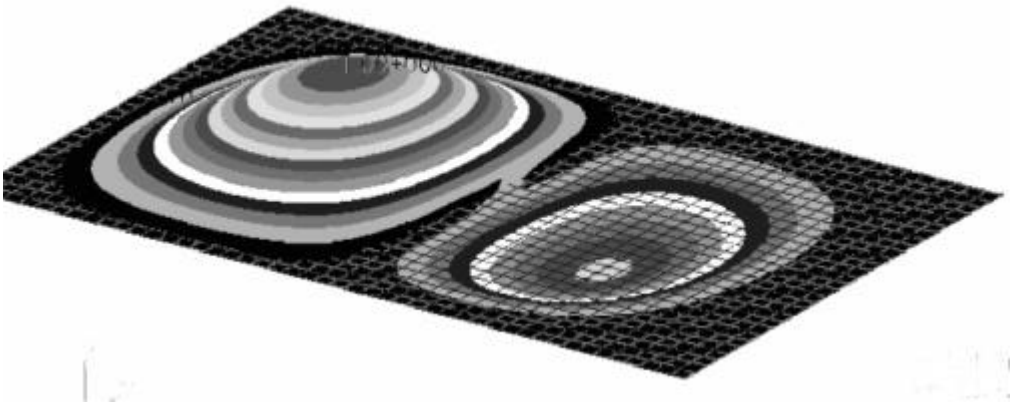

Figure 2 In-plane triangular (-1/-1/0) – CC.

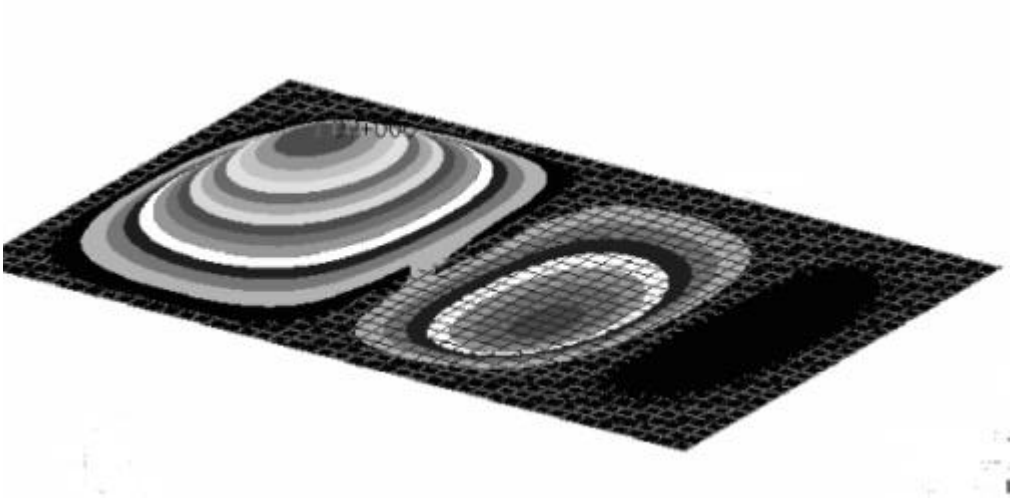

Figure 3 In-plane bending (-1/-1/0) – CC.

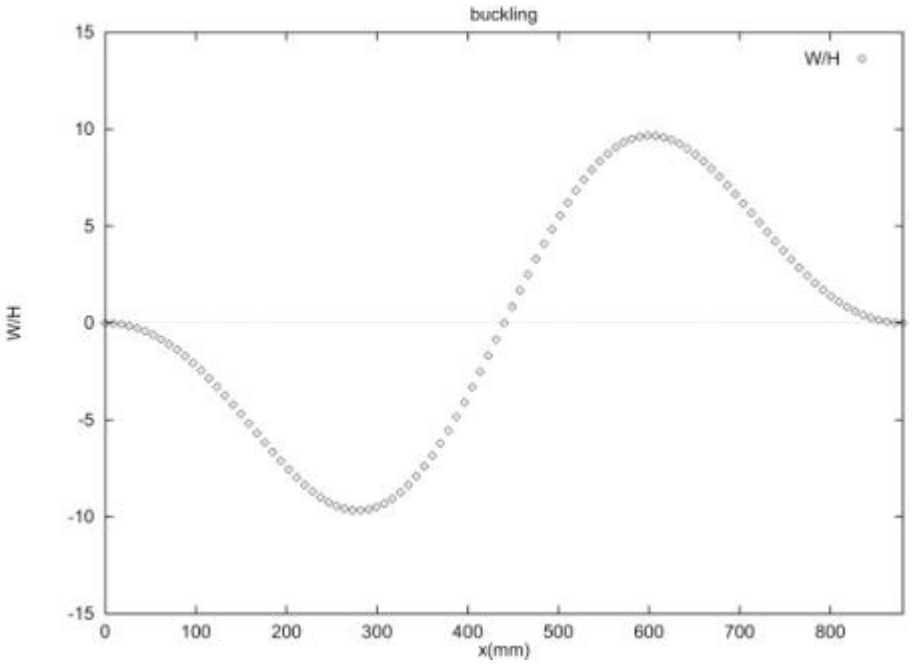

Figure 4 Uniform biaxial load (-1/-0.6/0) – CC.

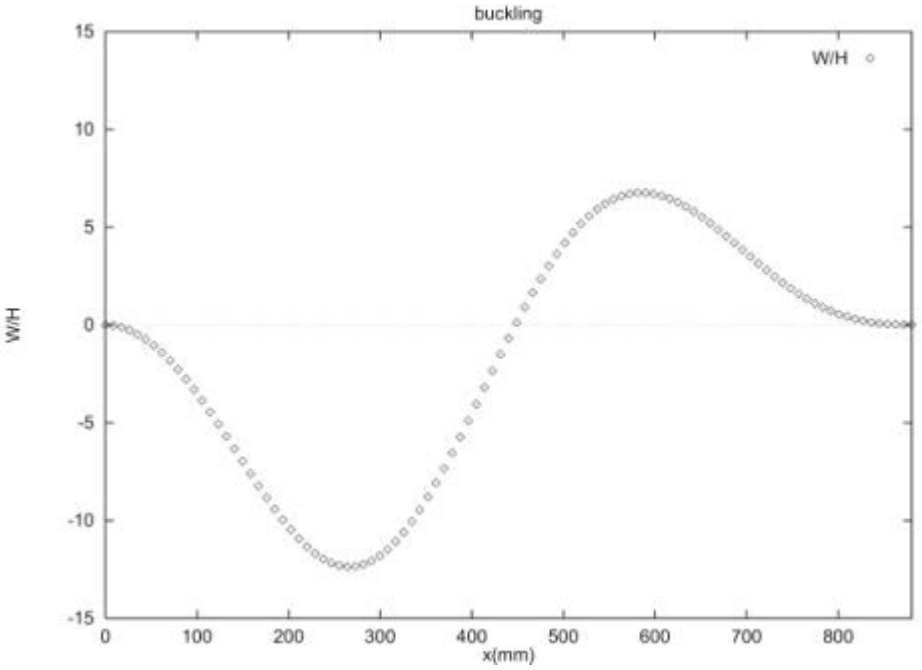

Figure 5 In-plane triangular (-1/-1/0) – CC.

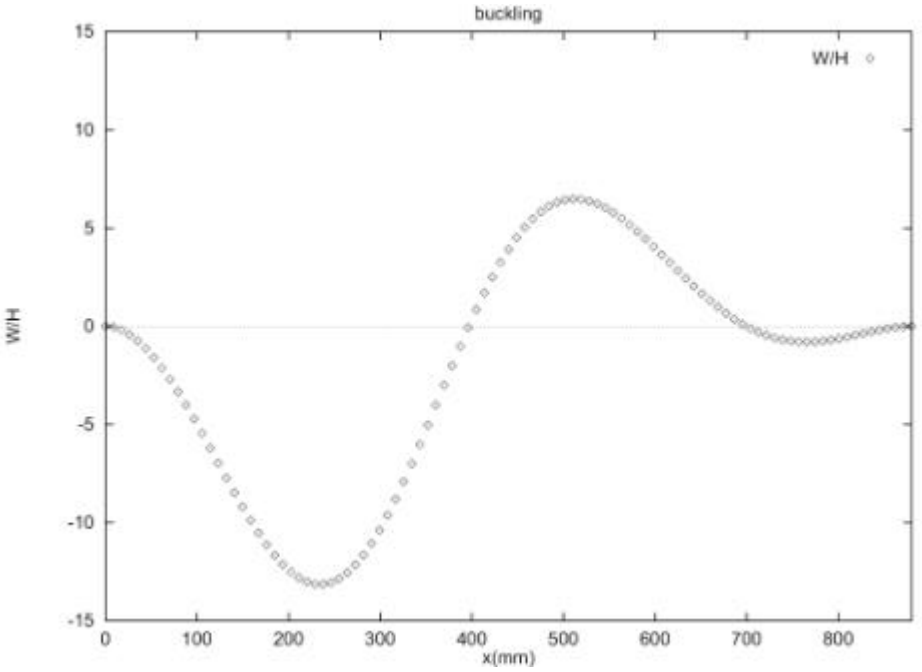

Figure 6 In-plane bending (-1/-1/0) – CC.

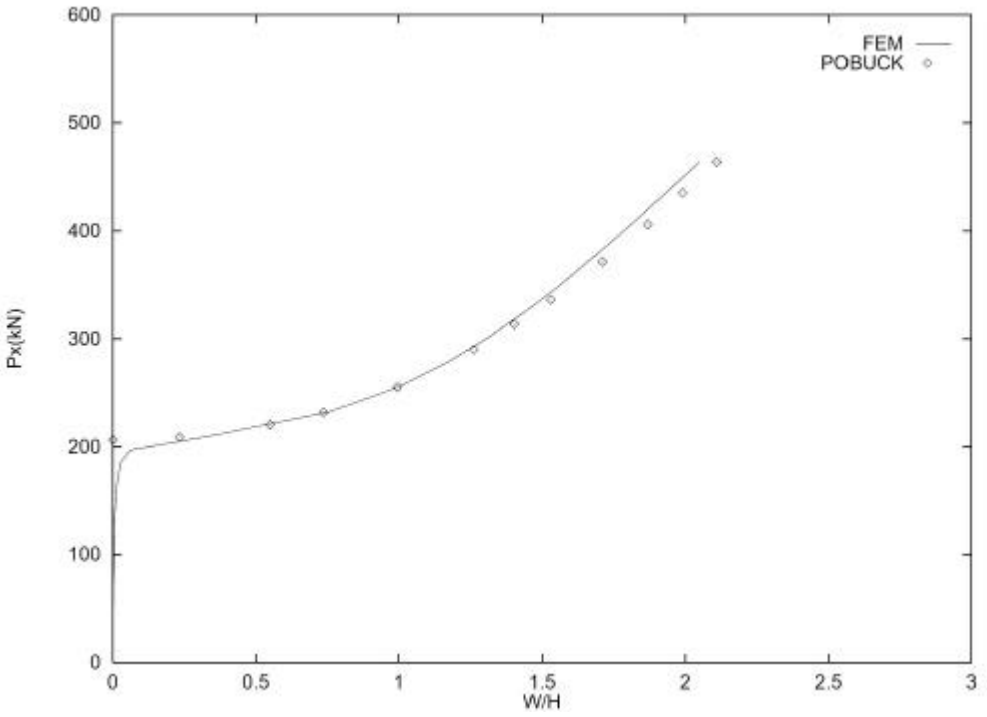

Figure 7 Load-maximum deflection behaviour (in-plane bending).

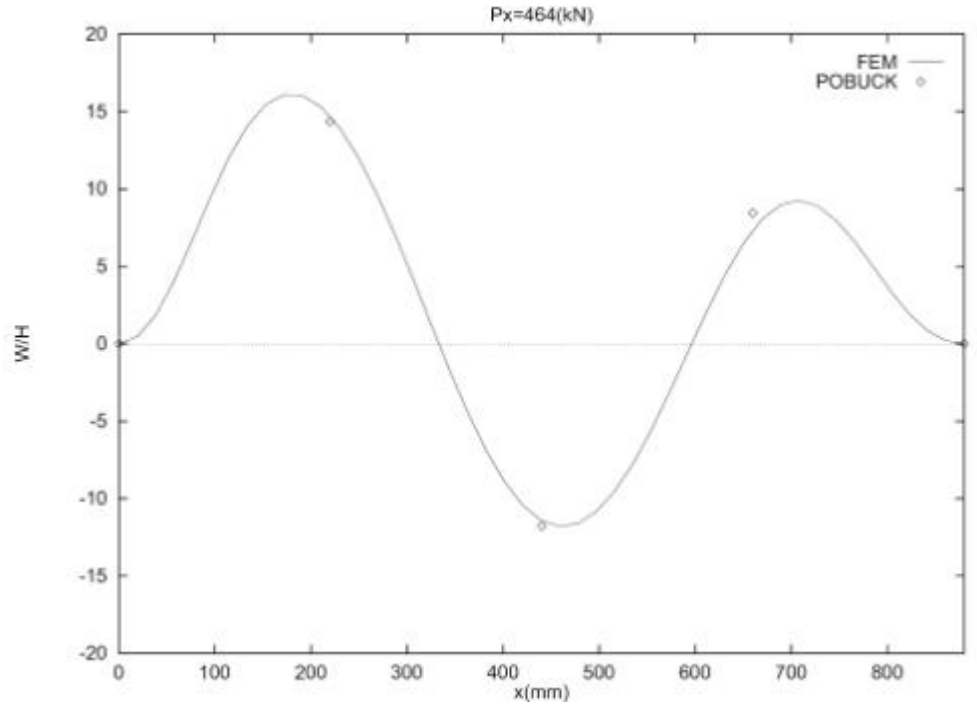

Figure 8 Longitudinal mid-plane deflection (in-plane bending).

ISSN 1590-8844
International Journal of Mechanics and Control, Vol. 06, No. 01, 2005

SPACECRAFT ATTITUDE CONTROL FOR EXTREMELY ACCURATE LINE OF SIGHT POINTING

Piergiovanni Magnani*, Amalia Ercoli-Finzi**, Franco Bernelli-Zazzera**

* Galileo Avionica

** Dipartimento di Ingegneria Aerospaziale, Politecnico di Milano

ABSTRACT

The paper addresses the design of the control system for very advanced in-orbit scientific and technological experiments that will require extremely accurate line of sight control of a pointing spacecraft with respect a target. The pointing performances are achieved by the utilization of accurate sensors, low disturbance actuators and the development of control schemes (dynamic modelling, data merging and control algorithms) which take advantage of state of the art technology. In this paper the simulation approach is presented, as well as the achieved results, when a relative alignment of two spacecrafts nominally co-orbiting in geostationary orbit is required to be better than some milliarcseconds. Suitable dynamic and measurement models and control methods are developed and demonstrate that the alignment can be obtained while oscillation jitters are maintained extremely low in the frequency band above a reference value of one Hz.

Keywords: relative attitude control, line of sight alignment, jitter

1 INTRODUCTION

The in orbit scenario taken as reference for the analysis is sketched in Figs. 1 and 2, and aims at a tentative approach to detect possible non symmetries of the fundamental space-time tensor caused by electro magnetic fields, e.g. unified fields theories [1].

As illustrated in Fig. 1, the experiment consists of three orbiting Spacecrafts (S/C): the Pointing S/C, the Target S/C and the Distorter S/C. The Pointing S/C, an extremely stable platform, needs to be optically aligned to a 'large detector' sensor placed at the Target S/C so that a highly collimated laser beam can form a 'spot' on such sensor. Upon activation of the electromagnetic fields at the Distorter S/C, the spot may be subject to feeble transversal displacements, which can be determined by centroiding techniques, providing an indication on the searched non symmetries. In Fig. 2 the nominal orbital and alignment frames for the Gun and Target S/Cs are illustrated, shown displaced from their ideal positions (coinciding with the origin of the frames).

Contact author: Piergiovanni Magnani

Galileo Avionica
Via Montefeltro 8 – 20156 Milano, Italy

Given the nature of the scientific investigation to be performed, the operational approach considered can be based on the following points [2]:

1. the Pointing S/C needs to be optically aligned onto the sensor surface array of the Target S/C for sequences of Basic Time Interval (BTI), each allowing the execution of a portion of scientific investigation. During each BTI a free drifting phase has to be guaranteed, that is the vibration on the Pointing S/C and Target S/C need be really minimum in order not to disturb the scientific measurement;

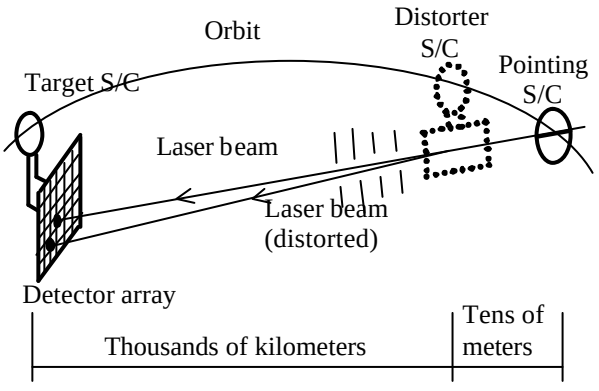

Figure 1 In orbit experiment schematics.

2. during BTI the Pointing S/C Line Of Sight (LOS) tends to drift away from the target because of the effects of non zero initial relative angular speed rate and the disturbance torques due to the radiation pressure and gravity gradient. Furthermore the Pointing S/C position, as well as the Target S/C position, tend to drift due to non zero initial speed rate, radiation pressure, Sun/Moon perturbations, Earth potential distortion terms;
3. after each generic BTI the actuators can be fired within a suitable Firing Time (FT), as schematized in Fig. 3, in order to generate the appropriate starting conditions for the Pointing S/C to properly initiate and allow the development of the next BTI by re-centering the Pointing S/C LOS to the Target S/C, and a recover the drifting attitude for the Target S/C, only with a coarse accuracy;
4. during the repetition of several combined 'BTI followed by FT' sequences, the S/Cs abandon their nominal locations (as schematically shown in Fig. 2). Once the displacements exceed some allowed limits the S/Cs position recovery can be performed. However such a recovery needs to be performed by adopting thrusters in the class 20 (mN) and in time periods not overlapping the scientific measurements.

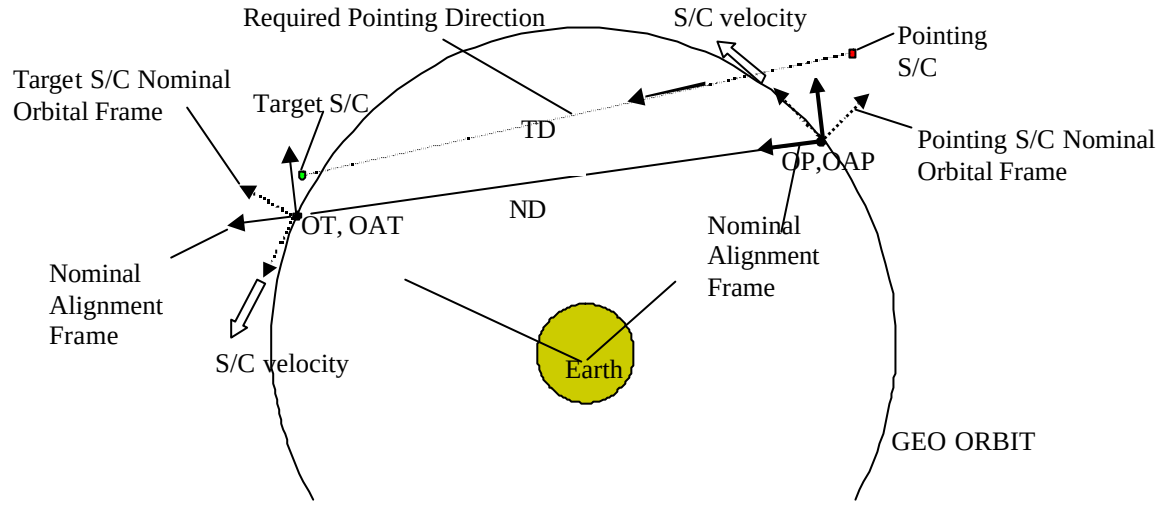

Note: OP, OAP, OT, OAT origin of the nominal orbital and alignment frames for the Pointing and Target S/Cs

Figure 2 Orbital configuration.

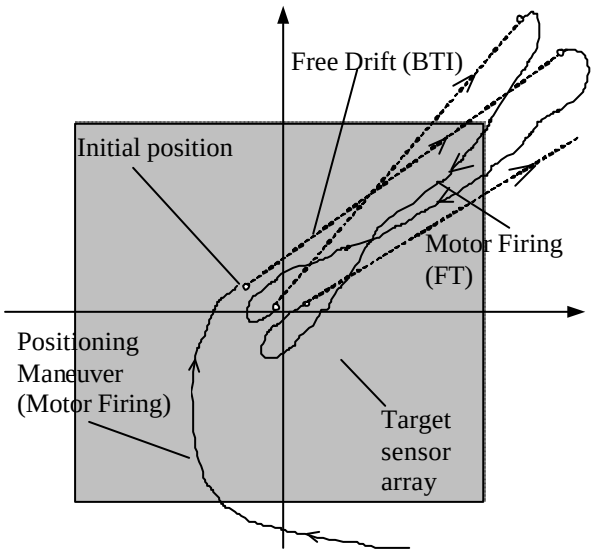

Figure 3 Relative pointing control strategy.

The Pointing S/C is the key element involved in the target acquisition process and it mounts the high accuracy sensors [2] and the ultra-fine thrusting actuator system ([3], [4]) necessary to the purpose. The Target S/C acts, in this respect, as a free drifting passive platform but for the laser beam casting so to implement the 'guide star' functions. The Distorter S/C, which is near to the Pointing S/C, will be controlled relative to the Pointing S/C in a 'coarse manner' and does not play a key role in the fine alignment process.
The feasibility of such a mission will depend, primarily, on the performances attainable during three specific phases: target acquisition with a very high accuracy, scientific phase that asks for a suitable time of permanence on target with very low jitter level, position recovery with the utilization of very low thrust actuators. In the following such phases are evaluated in detail in order to assess their feasibility.

2 POINTING S/C STRUCTURAL MODEL

The Pointing S/C structural elements utilized for the simulation are illustrated in Fig. 4 and include:

- inner optical platform carrying the high accuracy optical payload (relative attitude sensor interferometer, pointing laser, narrow field of view star tracker, metrology system) and gyroscopes;

- an outer structural frame carrying all remaining typical S/C sub systems (propulsion, power, thermal, TT&C, OBDH);
- two short appendages representing e.g. solar panels folded and locked, antennas, … .

The connection between the inner optical platform and the outer structure is modelled by means of 6 springs (3 linear, 3 angular) and 6 dampers (3 linear, 3 angular). The connection between each of the two appendages and the outer structural frame is modelled by means of 2 springs (1 linear, 1 angular) and 2 dampers (1 linear and 1 angular).

The Pointing S/C state vector is described by 38 components (32 needed to describe positions and speeds of the bodies and 6 needed as extensions, to describe the non white noise of the solar radiation pressure fluctuations).

The pointing spacecraft measurement vector includes the following types of measurements, all provided by sensors that represent state-of-the-art technology:

- relative yaw and relative pitch, from the high accuracy interferometer relative attitude sensor [2], which is not yet state-of-the-art but it is demonstrated [5] that it can be produced with state-of-the-art technology;
- absolute bank (from the high accuracy star tracker);
- position displacements from the nominal alignment frame, from the position determination system based on satellite laser ranging (SLR), transponding techniques, GPS;
- absolute angular rates (from rate gyros).

The thrusters are assumed connected to the outer spacecraft structure and a possible configuration layout is shown in Fig. 5; this schematics can be arranged to adapt to the final S/C outer body structural arrangements (e.g. by implementing finite angles reorientation).

3 DYNAMIC AND MEASUREMENT MODEL

For the objectives of the present analysis the system composed by the Pointing S/C and the Target S/C has been linearized and modelled around the nominal orbital configuration. Different models have been derived and, in the final configuration, the following set of equations (1) has been considered:

$$\begin{cases} \dot{p} = A \cdot p + B_1 \cdot p_1 + \sum_{i=2}^{i=7} B_i \cdot p_i & \rightarrow \text{Pointing S/C} \\ \dot{q} = E \cdot q + F_1 \cdot q_1 + \sum_{i=2}^{i=4} F_i \cdot q_i & \rightarrow \text{Target S/C} \\ y = C \cdot p + \sum_{i=1}^{i=4} D_i \cdot g_i(q) & \rightarrow \text{Measurements} \end{cases} \quad (1)$$

The *Pointing S/C dynamics* parameters are represented by: p=Pointing S/C state vector (38 states), p_1=nominal thrust control vector (6 controls), p_2=resolution thrust control vector (6 controls), p_3=Moon/Sun perturbation vector (3 elements), p_4=Earth perturbation vector (2 elements), p_5=Sun flux vector (1 element), p_6=gravity gradient torque (2 elements), p_7=noise vector (thrust and radiation flux, 12 elements). Matrices *A*, B_1, B_2, B_3, B_4, B_5, B_6, *and B7* are of consistent dimensions.

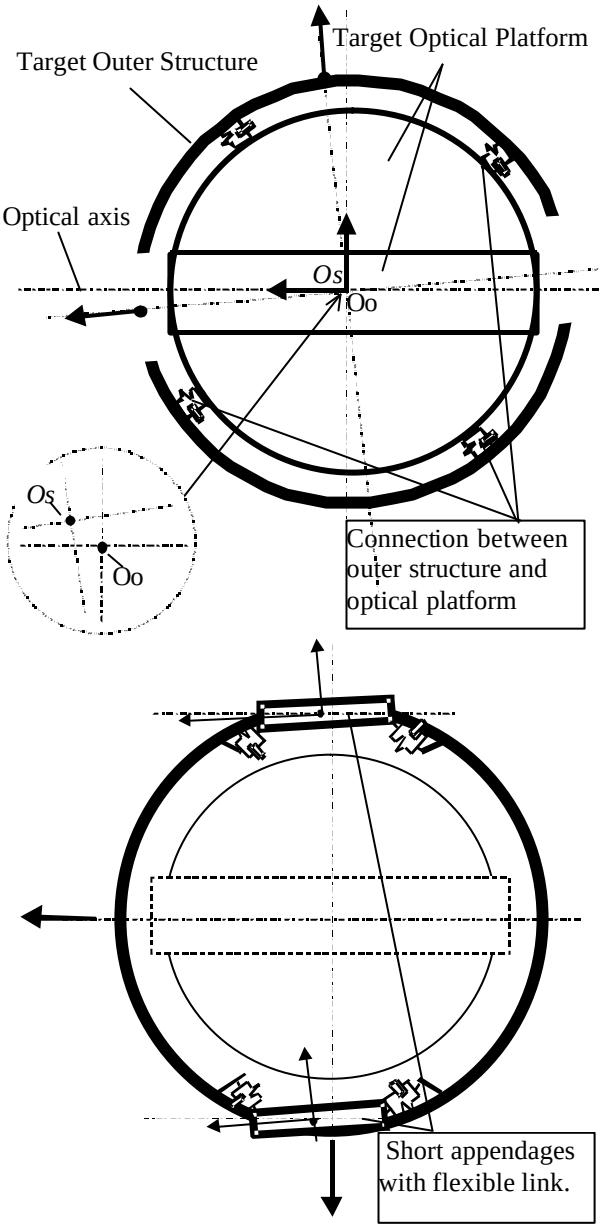

Figure 4 Pointing S/C structural schematics.

The *Target S/C dynamics* parameters are represented by: q=Target S/C state vector (6 states), q_1=nominal thrust control vector (6 controls), q_2= Moon/Sun perturbation vector (3 elements), q_3=Earth perturbation vector (2 elements), q_4=Sun flux vector (1 element). Matrices *E*, F_1, F_2, F_3, *and F4* are of consistent dimensions.

The *Measurements* parameters are represented by: y=measurement vector (9 elements), p=Pointing S/C state vector (38 states), g_1=attitude sensors offset vector (6 elements), g_2=forcing vector (3 elements), g_3=position sensors offset vector (3 elements) , g_4=measurement noise

vector (9 elements). Matrices *C*, D_1, D_2, D_3 and *D4* are of consistent dimensions.

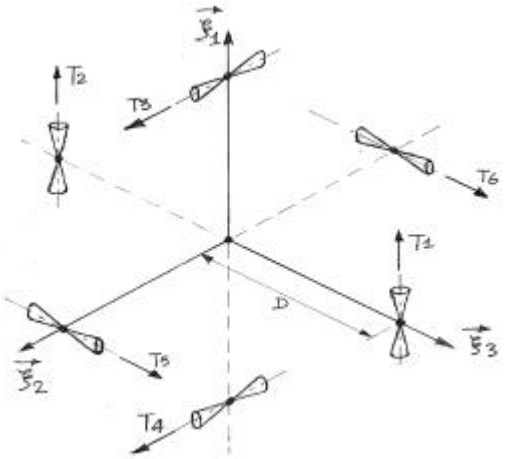

Figure 5 Schematics of possible thrusters arrangement.

As we can see the Target S/C has been assumed as an independently controlled, non cooperative platform whose coordinates *q* enter the measurement equations of the Pointing S/C. In turn the control loop of the Pointing S/C injects the information on the Target S/C position into the Pointing S/C dynamics via the regulator equations. The objective is to keep the Pointing S/C as much as possible relatively aligned to the Target S/C and with the minimum possible relative jitter.

4 CONTROL SCHEMES

In this section the basic control schemes utilized for the simulation of the pointing S/C dynamics are introduced. In all schemes the control is achieved by implementing loops based on six independent PID regulators. In particular, also with reference to Fig. 6, two PIDs are dedicated to the control of the relative attitudes (relative α and relative γ angles), one PID is dedicated to the control of one absolute attitude (β angle relative to the local alignment frame), and three PIDs are dedicated to the control of the position coordinates (x_p, y_p, z_p relative to the local alignment frame).

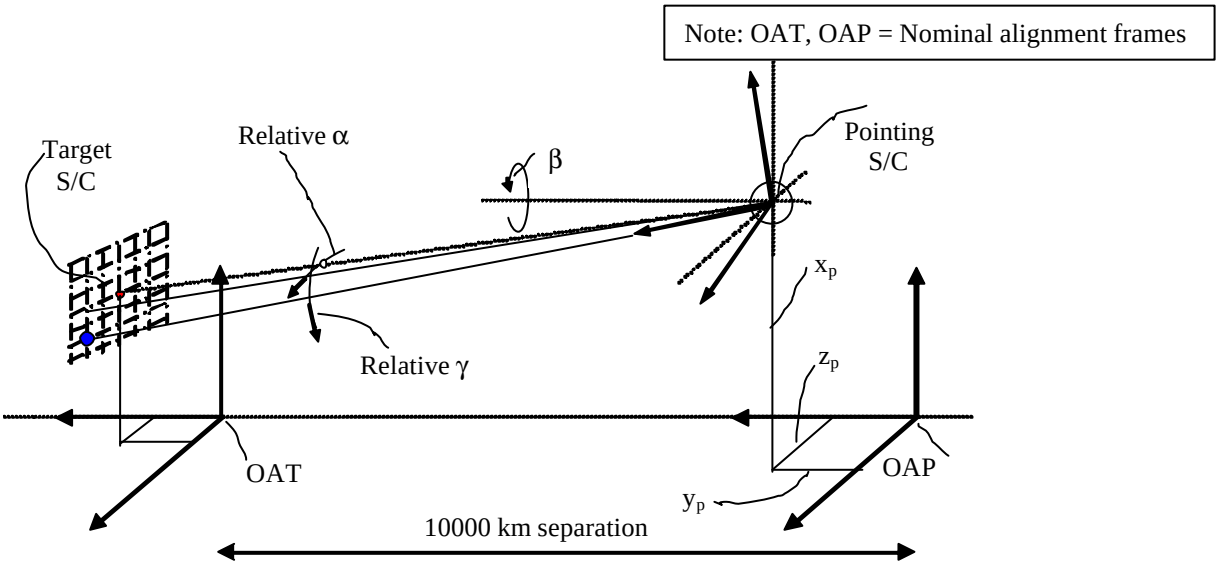

Figure 6 Schematics of the six controlled parameters (widely not to scale).

The control analysis has been carried out by considering two types of thruster systems used in different periods of the mission: a very accurate micro Newton class thrusters, limited to 100 μN and 300 μNm, dedicated to the relative target acquisition (and keeping) phase and a millinewtons class thrusters, limited to 20 mN and 60 mNm, dedicated to the position recovery phase.

During the relative target acquisition phase only the two relative attitudes and the absolute attitude are controlled by the micro Newton system while the position control is not active. In fact not only it is not needed by the mission but also the utilization of high thrust necessary for position recovery would induce strong disturbances in the relative pointing/alignment. During the position recovery phase instead, the micro Newton thrusters are not active since they would not be of any effect while the control is performed in all six coordinates.

4.1 CONTROL SCHEME FOR RELATIVE TARGET ACQUISITION (AND KEEPING)

The basic control scheme utilized is shown in Fig. 7, with the position control not active, and it is based on Kalman Filter (KF) implementation. Two characteristic control times are considered in the simulation: an interval δ for the

simulation of the dynamics and KF propagation and an interval Δ, typically one order of magnitude greater than δ, for the simulation of the control loops, the attitude/position sensors acquisition (relative attitude interferometer, high accuracy star tracker and position measurement system even if not used in this scheme) and KF update.

Concerning the KF implementation, the following considerations are noted:

1. the system distribution matrices, the radiation pressure average disturbances, the measurement matrix and some forcing parameter in the measurement equation have been implemented with inaccuracies; indeed 21 perturbing parameters are present directly affecting the attitude behaviour;
2. the system dynamic matrix has been assumed strongly perturbed in two primary stiffness parameters to simulate partial structural failure during launch.

Above perturbations have two types of effects at the level of performances considered: the perturbations of type a) create some relative attitude offsets (in the order of 0.01 arcsec) in the KF state reconstruction showing minor sensitivity while the perturbations of type b) are more important and tend to make the KF unstable showing an important sensitivity.

To cope with the above situations the following approach has been used:

1. the minor offsets have been controlled by implementing an integration action within the KF structure (see also eq.2);
2. the strong sensitivity to uncertainties in the dynamic matrix have been controlled by extending the KF to the uncertain parameters; the KF becomes then non linear so it has been linearized [6].

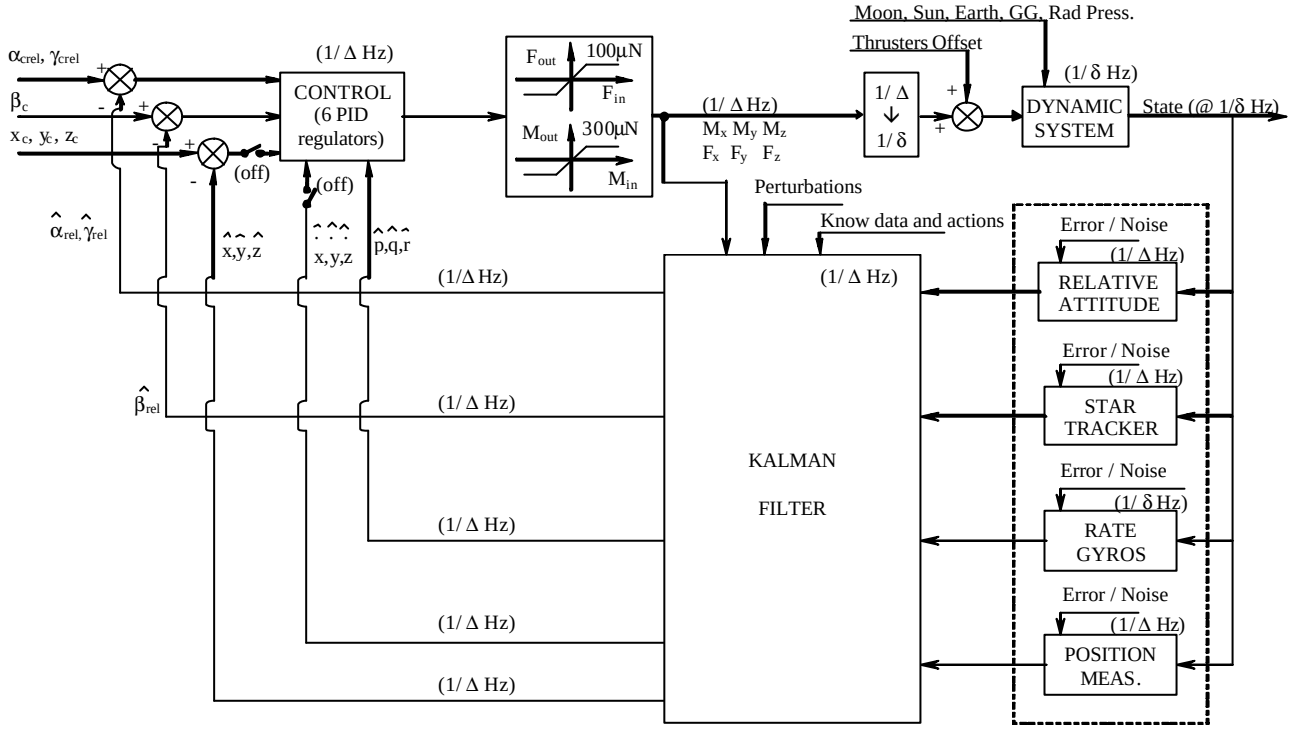

Figure 7 Control scheme for target acquisition and keeping.

The approach utilized allows a robust estimator with no need of an excessive extension of the filter. Other methods like 'memory loss' can indeed control the instabilities due to dynamic matrix uncertainties but the relative attitude errors increase to approximately 0.02-0.03 arcsec and the jitter in the band >1 Hz increases by a factor of 50 which is to be avoided for the specific application considered.

Typically, for the simulations, δ=0.01 (s) with sensitivity testing carried out at lower times (e.g. 0.0025 s, 0.001 s) and Δ = 0.5 (s) with sensitivity testing carried out at larger times (e.g. 2 s). It is noted that although the commanded forces (Fxc, Fyc, and Fzc) are zero, the actual forces exerted by the thrusters are not zero because of the practical imperfections involved (positioning, alignments, mismatch, …).

The gains of the regulators have been selected based on two approaches: tuning of gains with 'trial and test' (e.g. placement and regulation of proportional gains followed by placement and regulation of derivative gains and integral gains with iterations) and utilization of deterministic optimum control techniques [7] to derive proportional and derivative gains of comparable regulators.

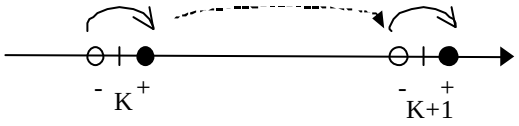

1 – State propagation

$$\hat{x}(k+1)_- = \Phi \cdot x(k)_+ + \overline{F}$$

2 – Measurement

$$z(k+1) = M \cdot x(k+1) + G + W$$

$$\hat{z}(k+1)_- = \overline{M} \cdot \hat{x}(k+1)_- + \overline{G}$$

3 – State update (2)

$$\hat{x}(k+1)_+ = \hat{x}(k+1)_- + K_{k+1}\{z(k+1) - \hat{z}(k+1)_-\}$$

4 - Added integration action

$$I(k+1) = I(k) + \{z(k+1) - \hat{z}(k+1)_+\} \cdot (t_{k+1} - t_k)$$

5 – Correction of State update

$$\hat{x}_C(k+1)_+ = \hat{x}(k+1)_+ + GI \cdot I(k+1)$$

4.2 CONTROL SCHEME FOR POSITION RECOVERY PHASE

During the recovery phase relative large amount of position displacements are to be managed, typically tens or hundreds of meters in the case considered. A control scheme which utilizes the final commanded coordinates directly in the control loop can require large time of stabilization if the control has very limited action capabilities (e.g. non linear control caused by small saturation thresholds like in our case). In such circumstances speed limitations may be needed otherwise the regulation action of the PID could require several passages near the final reference coordinates to damp the oscillations. An alternative and more deterministic approach can be devised taking as examples the "trajectory generation techniques" also used in other branches of engineering (like robotics).

With such an approach smooth reference trajectories can be planned with polynomial profiles compatible with the characteristics of the actuators and the desired quality of motion. For the specific case a quadratic generation has been considered for each of the six controlled co ordinates.

The recovery manoeuvres are implemented in two steps (see also Fig. 8 for a generic coordinate S): during the first step a speed damping (till zero) is achieved, in the second step the position is recovered to the nominal zero coordinate (and zero speed). For each step the process is the following:

- an initial sensor reading is performed;
- for each of the coordinates a minimum required manoeuvre time is computed compatible to both the target coordinate and a selectable amount of thrust/torque not to exceed; in such a way a due extra amount of force/torque is still available for the regulation actions (external disturbances compensations, specific regulation, …);
- the longest of the six times is taken as reference and the six profiles are generated anew by using this reference time;
- the six profiles are then passed to the system controller.

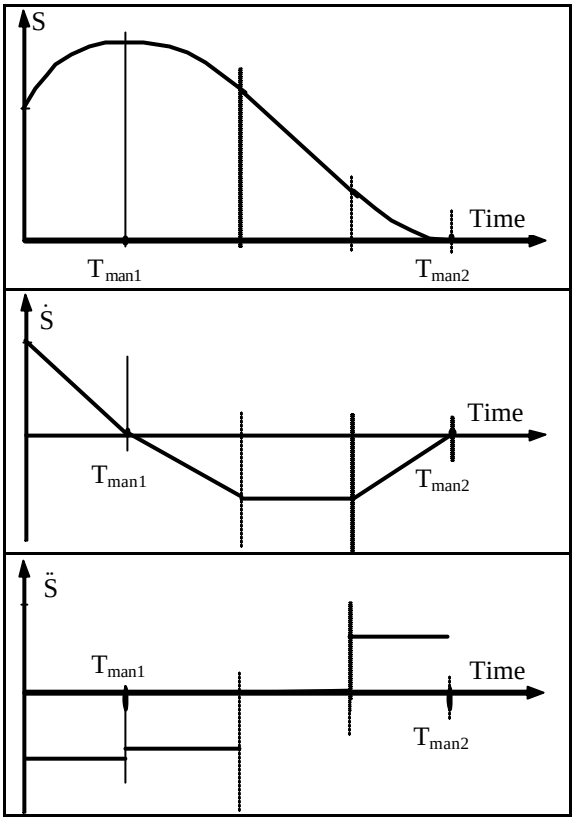

Figure 8 Example of generation of recovery profile.

The selection of the parameters used for the trajectory profile generation affects primarily the time of manoeuvres and the electric power requirements, to a lesser extent the fuel consumption. The gains used in the control loop, related to the allowed errors during manoeuvres, affect the fuel consumption; optimum determined gains from linear theory are considered. However it has to be said that the closed loop system very easily becomes non linear (due to the forces saturation) as soon as the manoeuvre is tried to be faster.

The approach considered allows performing stable, reliable and fuel limited recovery manoeuvres.

A schematic of control loop for the recovery phase is shown in Fig. 9 and realizes the control on all axes (positions and attitudes). It has been simulated by considering a relative attitude sensor with characteristics typical of an absolute high accuracy star tracker and by considering actuators of Xenon type capable of thrust level compatible with this type of mission. The obtained performances are representative of an absolute control in the nominal alignment frame.

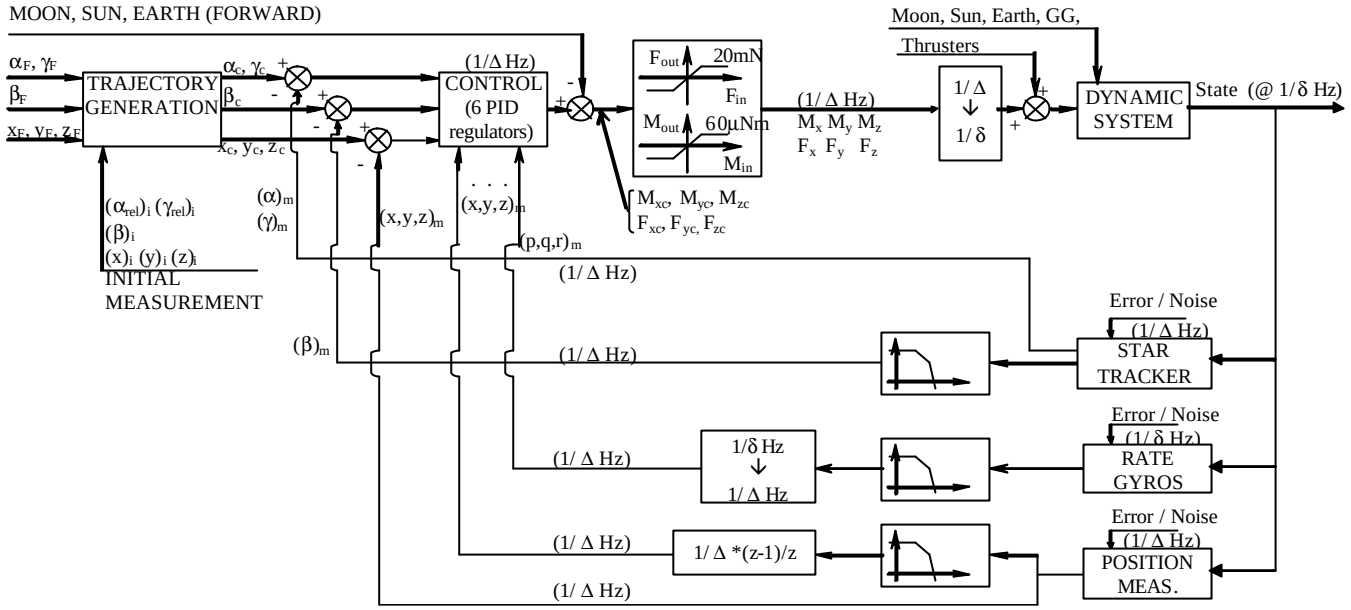

Figure 9 Basic control scheme for the position recovery phase controller.

5 NUMERICAL SIMULATIONS AND RESULTS

Several simulations have been carried out for the three key mission phases: target acquisition and keeping, scientific phase (both repeated acquisitions and free drifts) and position recovery.

Concerning the target acquisition and keeping phase, the main objectives were to evaluate the pointing accuracy and jitter. During the analysis, large initial misalignments and Target S/C high drifting speeds have been assumed in order to assess the capability and the necessary time for correct Target acquisition and tracking. Furthermore, particular importance has been given to robustness of the closed loop system against inaccuracies and perturbations for the distribution, measurement and system matrices.

The evaluations performed on the scientific phase had the main objectives to estimate the time of permanence of the LOS onto the Target S/C (indeed on its large sensor array) and the residual jitters for different levels of external disturbances. The robustness of the closed loop system against Target S/C strong perturbations during repeated target acquisition steps have been assessed.

The evaluations performed on the position recovery phase aimed at the overall verification of the recovery strategy based on trajectory planning techniques. On top of the basic feasibility aspects, two major indicators have been explored: fuel consumption and power consumption. Several parameters have been varied including geometry of the commanded trajectory, reference maximum accelerations, allowed errors during trajectory execution (selection of the control gains).

In this section, to get an overview of the achievable performances, some of the obtained simulation results are presented for the three investigated phases.

5.1 TARGET ACQUISITION AND KEEPING PHASE

Figure 10 presents a sample of performances concerning the relative attitude angles: pitch (relative γ) and yaw (relative α). The target acquisition manoeuvre starts from an initial combined relative attitude of 2.5 arcsec and a relative attitude speed of 0.006 arcsec/s since a fast moving target with initial speed of 0.3 m/s has been assumed. Furthermore a strong target stepwise position perturbation (70 m combined) has been injected to check for the tracking capability of the system. The results evidence that the acquisition and tracking capability is fairly effective and robust, stabilizing in about 200 s. Furthermore the pointing error, over a stabilized observation window, is approximately 0.005 arcsec of which about 0.0025 arcsec are the basic offset of the relative attitude sensor. This correspond to approximately 0.25 m at the target plane. The combined jitter in the band above 1 Hz is about 2 arcsec rms which corresponds to approximately 1E-6 m rms at the target plane.

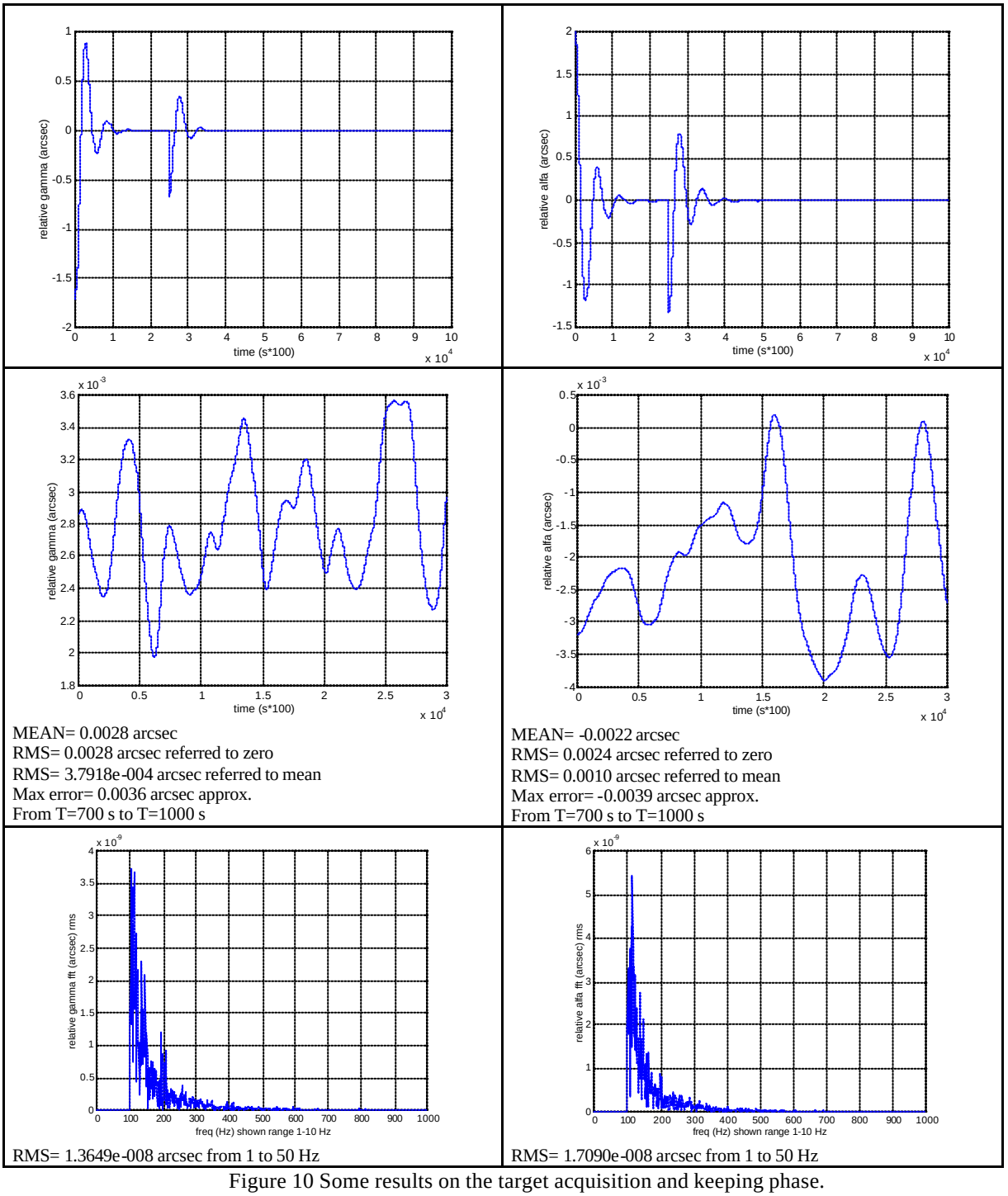

Figure 10 Some results on the target acquisition and keeping phase.

5.2 SCIENTIFIC PHASE

Figure 11 summarizes some key performances during the repeated acquisition sequences during Scientific phase. For this simulation the allowed drift distance from the centre of the target was set to 12 m above which the target acquisition was restarted. The overall phase is therefore an alternate sequence of target acquisition and free drifts. The control system has been proved very robust against sensitivity verifications (S/C optical properties unbalance, radiation pressure fluctuations, target geometry size, position perturbations on the target S/C) and the following considerations are noted:

- with the set parameters one complete cycle is performed in approximately 200 s;
- the free drift phase last for approximately 50-60 s during which the core of the scientific experimentation can be done;
- the total fuel consumption in 1.5 years, assuming a duty cycle of scientific phases versus position recovery

phases of 1:2 turns out to be of 0.007 kg of propellant (caesium or indium for the FEEP technology).

The jitter behaviour above 1 Hz during the free drift phases is summarized in Fig. 12. It is noted that jitters on target plane better than 1E-10 m = 0.0001 μm are achievable and even assuming uncertainties of 100-1000 on the PSD value of the radiation pressure fluctuations, the jitter would remain more than one order of magnitude smaller than a value of 0.1 μm which could represent a reference resolution on the laser spot centroiding determination.

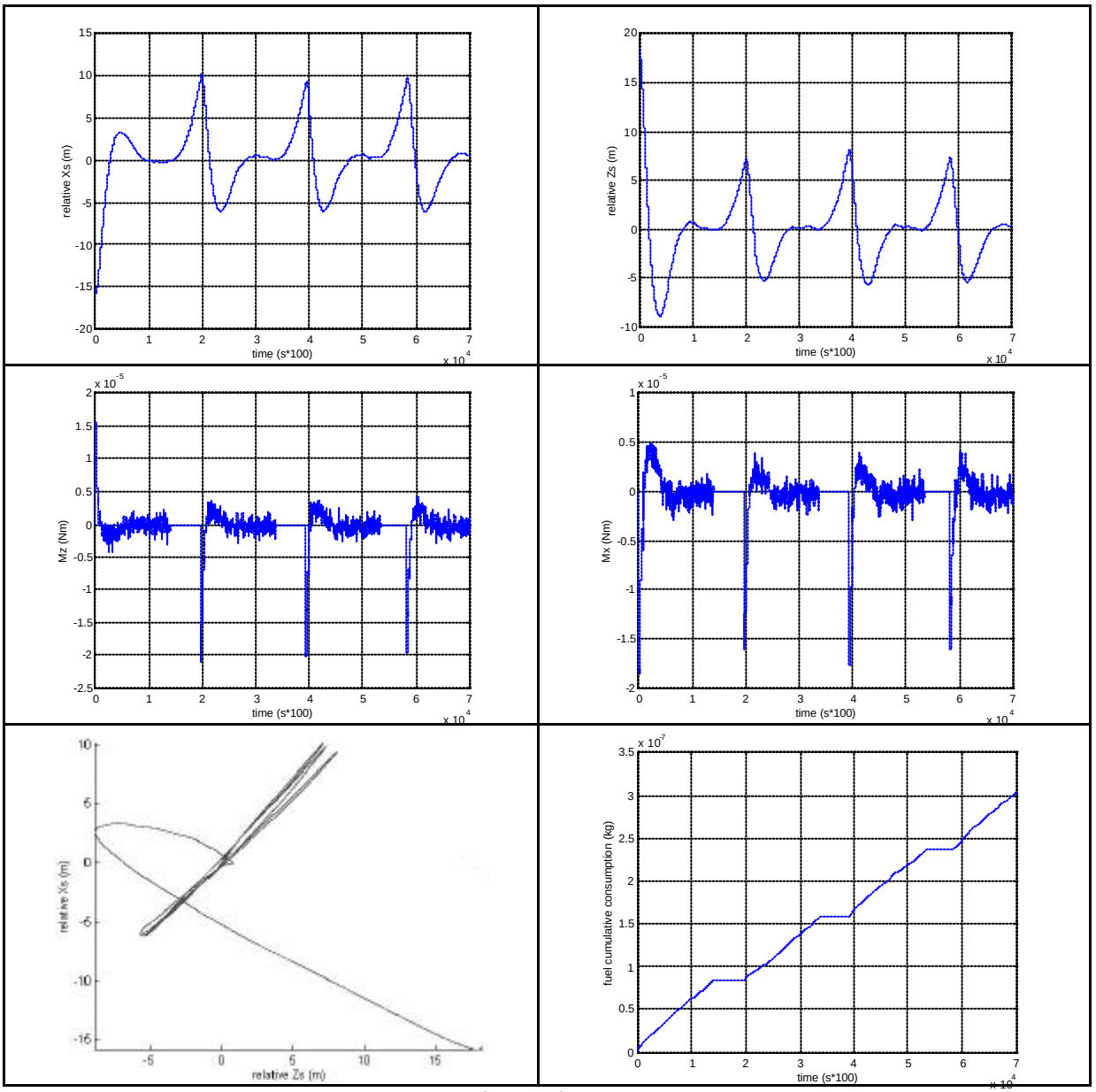

Figure 11 Example of scientific phase, repeated acquisition.

5.3 POSITION RECOVERY PHASE

Figure 13 summarizes some representative results related to a recovery phase. The behaviour of the system is time variant since it depends on the relative Earth-S/C-Moon-Sun positions. In the case shown a kind of worst case situation has been considered since the starting conditions have been assumed around the full alignment of the bodies involved.

The recovery starts from an initial position offset of about 330 m and initial speeds which would accumulate from a previous Scientific phase lasting in the order of three hours. The first step of the recovery manoeuvre takes about 8113 s and slows down the S/C motion to zero speed while the position error would grow to about 600 m; the second step lasts about 14006 s and would bring the S/C to its zero position with zero speed ready to start a new scientific phase.

The total fuel consumption for the recovery, in the assumed conditions, results approximately 0.021 kg, which would lead for a 1.5 years mission to approximately 30 kg of fuel (e.g., xenon). Concerning the electric power consumption, it presents an average value of 920 W with sustained period of 1400 W which will pose due requirements on the Power and Distribution System.

While the time is evolving, the perturbation effects from the Sun and Earth are continuously changing, but we can assume the case reported representative for the feasibility of the manoeuvre.

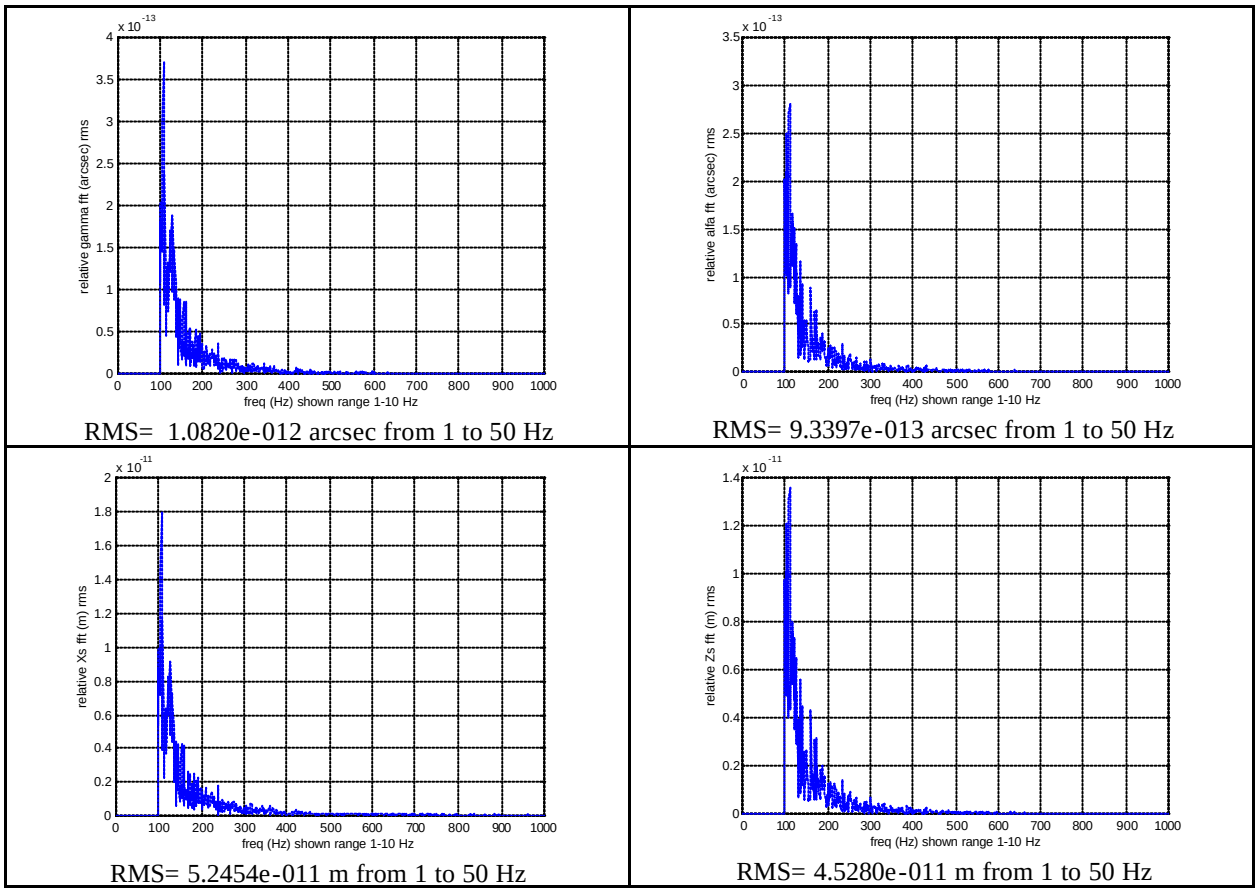

Figure 12 Example of scientific phase, free drift (scientific measurement).

6 CONCLUSIONS

The extraordinary possibilities offered by the space environment and the progressive improvements in space related technologies open to new potential scenario for in orbit experimentation related to basic physics issues.

The results presented in this paper, based on appropriate dynamic modelling and control system, proved that LOS relative control of a Pointing S/C to a distant Target S/C can be achieved with very high performances. In fact for two reference S/Cs in GEO at a nominal distance in the order of 10000 km, a Target S/C interception error of 0.25 m (relative pointing error of ~ 0.005 arcsec) with Target S/C interception jitter of 2 μm appears feasible during sustained target acquisition. When the alignment is reached and stabilized the Line of Sight relative jitter will drop to something in the order of 0.0001 μ m if the relative control is switched off leaving the S/Cs in free drift mode.

A very important issue in order to achieve above performances is the on board availability of direct relative attitude measurements with performances far below the arcsec level and ultra low noise thrusters. On line dynamic filtering appears furthermore to be quite effective and can be brought robust enough with respect to the modelling uncertainties (distribution matrices, dynamic matrix, and measurement matrix).

With respect to the in orbit operation scenario shown in Fig. 1, taken as reference for the analysis, the key issue of extremely accurate and stable relative alignment of the Pointing S/C on to the Target S/C appears to be achievable.

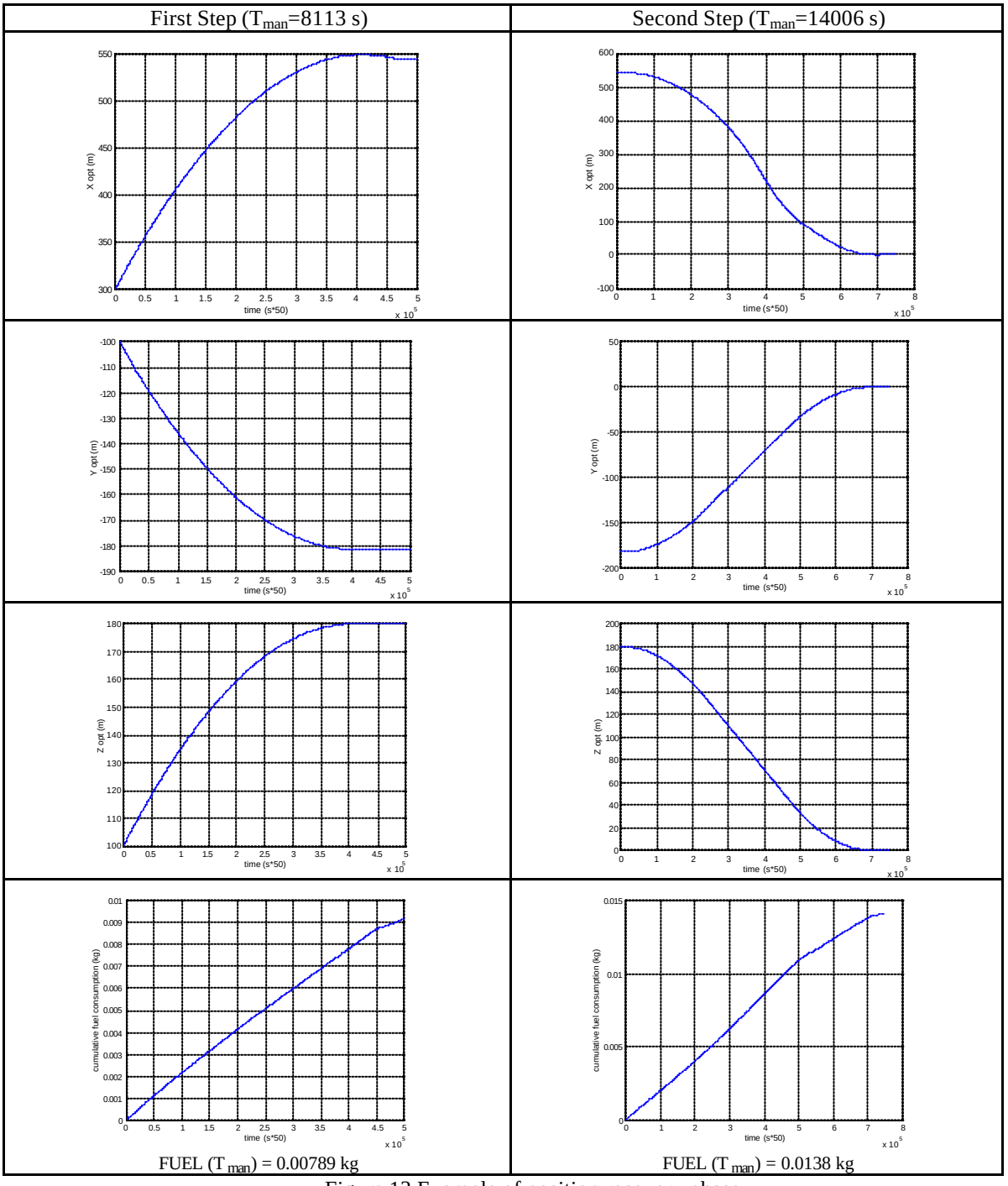

Figure 13 Example of position recovery phase.

REFERENCES

[1] Magnani PG. and Finzi A.E., A Possible In Orbit Relativistic Experiment Mission with Very Accurate S/C Relative Control. *Aerotecnica Missili e Spazio*, Vol. 83, No. 2, pp. 77-84, 2004.

[2] Magnani PG., *Methodologies for accurate spacecraft relative control in support to very demanding scientific missions*. PhD Thesis, Politecnico di Milano, 2004.

[3] Tajmar M., Genovese A. and Steiger W., Indium field emission electric propulsion microthruster experimental characterization. *Journal of Propulsion And Power*, Vol. 20, No. 2, pp. 211-218, 2004.

[4] Marcuccio S., Genovese A. and Andrenucci M., Experimental performance of field emission microthrusters. *Journal of Propulsion And Power*, Vol. 14, No. 5, pp. 774-781, 1998.

[5] Magnani PG. and Bernelli Zazzera F., Wave front interferometric technique for accurate spacecraft relative attitude determination. *Optical Engineering*, Vol. 44, No. 2, 2005.

[6] Gelb A., Kasper J.F., Nash R.A., Price C.F. and Sutherland A.A., *Applied Optimal Estimation*, the M.I.T. Press, 1986.

[7] Friedland B., *Control System Design: an Introduction to State Space Methods.* McGraw Hill, 1986.

ISSN 1590-8844
International Journal of Mechanics and Control, Vol. 06, No. 01, 2005

ALL WHEEL DRIVE COMPONENTS MODELLING AND THEIR INFLUENCE ON VEHICLE DYNAMICS

Aldo Sorniotti

Department of Mechanics, Politecnico di Torino

ABSTRACT

The goal of the activity consists in modelling the most commonly used active and passive differentials, and in the evaluation of their influence on vehicle dynamics. The models here presented are not only functional models, giving origin to precise output torques/speeds in correspondence of defined inputs, but they describe the internal way of work of the components. They can be used for a predictive analysis. First of all, the model of a Haldex® differential is presented; both the mechanical and the hydraulic components are described in detail. A similar work is carried on for Torsen® T1 and T2 differentials, GKN Visco-Drive® device and Powr-Trak® differential. The influence of each friction coefficient and the configuration of the gears on the overall component behaviour is evaluated. All these models are inserted inside a vehicle model, to give origin to different configurations of All-Wheels-Drive (AWD) systems. A comparison is performed at different open throttle conditions, with a big variety of steering wheel inputs, like step steer, double step steer, ramp steer. Evaluation criteria to analyse the results are presented.

Keywords: All-Wheels-Drive systems, models, vehicle dynamics

1 INTRODUCTION

Nowadays, AWD vehicles are obtaining an increasing success in the market. A lot of different solutions have been put in production. The most difficult task for the powertrain and driveline engineer consists in understanding which are the real advantages of each solution. Simulation appears to be the most objective and cheap way.

2 HALDEX® DIFFERENTIAL

Haldex® differential is one of the most innovative products. It is governed by a control strategy contained in an Electronic Control Unit. The main advantage of an active differential over a passive differential is the chance of regulating not only the longitudinal slips between the two axles, but also the lateral dynamics of the vehicle, with a reduction of understeer/oversteer phenomena.

Contact author: Aldo Sorniotti

Department of Mechanics, Politecnico di Torino,
Corso Duca degli Abruzzi 24 – 10129 Torino, Italy
E-mail: aldo.sorniotti@polito.it

The second advantage is the easy integration with Electronic Stability Program (ESP), nowadays adopted on most European vehicles. Haldex® differential can be used in the central location and can vary the torque distribution between front and rear axles. In typical applications, it is possible to make vary the torque to the rear axle from 0% to 50% of the total torque from the engine. The typical usage of this differential can regard the transformation of a front wheel driven car in an AWD vehicle. The engine transmits the torque to the front differential via the gearbox. The direct connection of the gearbox to the front differential permits transmitting a defined percentage of the total torque to the front axle, depending on the central differential.
A gear (located in correspondence of the front differential external box) permits the transmission of the motion to a shaft, entering, in correspondence of the rear side of the vehicle, Haldex® differential. Haldex® clutches transmit the torque to the rear differential. It is improperly defined as a differential, since it is characterized only by a single mechanical input port and a single mechanical output port. Figure 1 shows a typical configuration of the differential on a car.

Figure 1 The Haldex® differential mounted
in the rear side of the car as a central differential

Haldex® electronic unit receives as inputs the signals from the sensors in the car, for example wheel speed sensors and gas throttle position. Haldex® Electronic Control Unit (ECU) is connected to CAN (Controller Area Network); the received signals are the same used by the ESP. On this basis, the ECU decides the torque which has to be transmitted to rear axle by the clutches of the differential. Haldex® differential (Figure 2) consists of a mechanical part, a hydraulic part and an electrical part. The mechanical part is formed by a multi-disc clutch (Figure 3), capable of limiting the relative slip between input and output shafts; for this reason, Haldex® differential can be included in the class of the Limited Slip Differentials (LSD). The clutches are inside oil; the transmission of the torque does not depend, like in other differentials, on the viscous coefficient of a devoted fluid. In Haldex® differential, torque is transmitted by Coulomb friction, with a low consumption of the discs. From a theoretical point of view, Haldex® differential could work to limit the relative speed between input and output shafts only thanks to its hydraulic circuit, without the control unit. It is characterized by a cam, rotating together with the output shaft and by some rollers, restrained to the input shaft. The frame of the differential prevents the rotation of the three pistons of Figure 4. Two of them are located on the rollers; the relative motion of input and output shafts provokes an axial motion of these pistons giving origin to a pumping effect. It is generated an oil flow rate to the third piston (the working piston), provoking the compression of the clutches. Pumping pistons are equipped with a system of uni-directional valves, at the input and output ports, to prevent oil reflux. This is the basic principle of Haldex® differential. Simulation activity demonstrated the complexity required for the design of such a system, since the cams, if not properly defined, can generate very high peak values of pressure inside the hydraulic circuit. In some applications of Haldex® differential, a third cam is used to determine the displacement of the working piston, to attenuate the pressure fluctuations provoked by the other two cams. Of course, the control unit improves the behaviour from the point of view of pressure fluctuations and the possible integration with ESP. Torque transmission does not depend only on the relative speed between output shaft and input shaft, but also on vehicle dynamics. To obtain this result, Haldex® hydraulic unit consists also of a pump, driven by an electric motor, a spring accumulator, and a regulation valve.

Figure 2 Haldex® differential

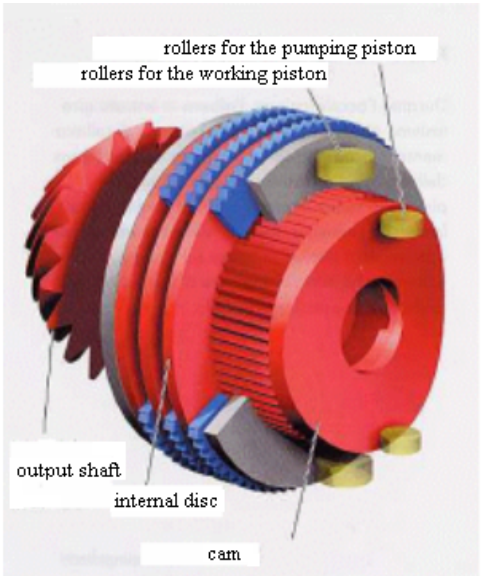

Figure 3 Main hydraulic components
of a Haldex® differential

These are the components permitting the active control of the differential. The valve, controlled by the software, can be regulated by a moto-positioner or by a solenoid, according to the application of the differential.

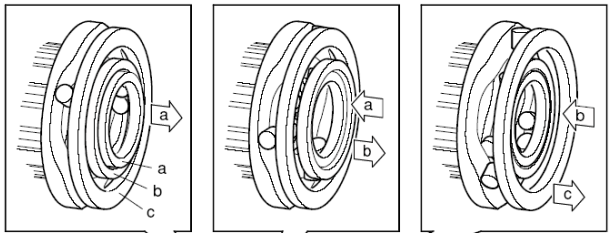

Figure 4 a, b: pumping elements of Haldex® differential; c: working piston

The pump, also when the regulation valve is fully open, maintains a pressure level of 4 bars, to pre-charge the discs. This work permits a reduction of time delays in the case of a sudden request of torque through the system. The maximum pressure level inside the hydraulic circuit is about 70 bars; above that value, a pressure limiter valve puts in communication the hydraulic circuit with the oil reservoir, corresponding to the carcass of the differential. The regulation valve is located between the pump outlet port and the oil tank in the carcass. The valve can be used to make pressure vary inside the hydraulic circuit, both to reduce and increase the level imposed by the pumping elements. To optimise actuation, devoted sensors are located in proximity of the regulation valve, to measure pressure and temperature levels. Temperature level is particularly important, since its variation can determine a consistent change in oil viscous properties. The larger is the temperature, the larger will be the opening level of the regulation valve to obtain the same effect.

A specialized software, AMESim®, for modelling hydraulic and mechanical systems, was used to model Haldex® differential. Figure 5 is a sketch of the model; it is possible to observe the clutches, the pumping elements, regulated by the cam displacement, the working piston (acting on an equivalent spring), the motor pump, the accumulator, the pressure limiter valve and the regulation valve. The model permits to evaluate the influence of each parameter on the whole system; for example, it is possible to predict pressure variation as a consequence of different fluid viscosities or cams shapes. Also the internal oil flow rates can be computed by the model. For example, in Figure 6 lines 1 and 2 are the flow rates from the pumping pistons, 3 is the flow rate through the working piston and 4 is the flow rate through the regulation valve.

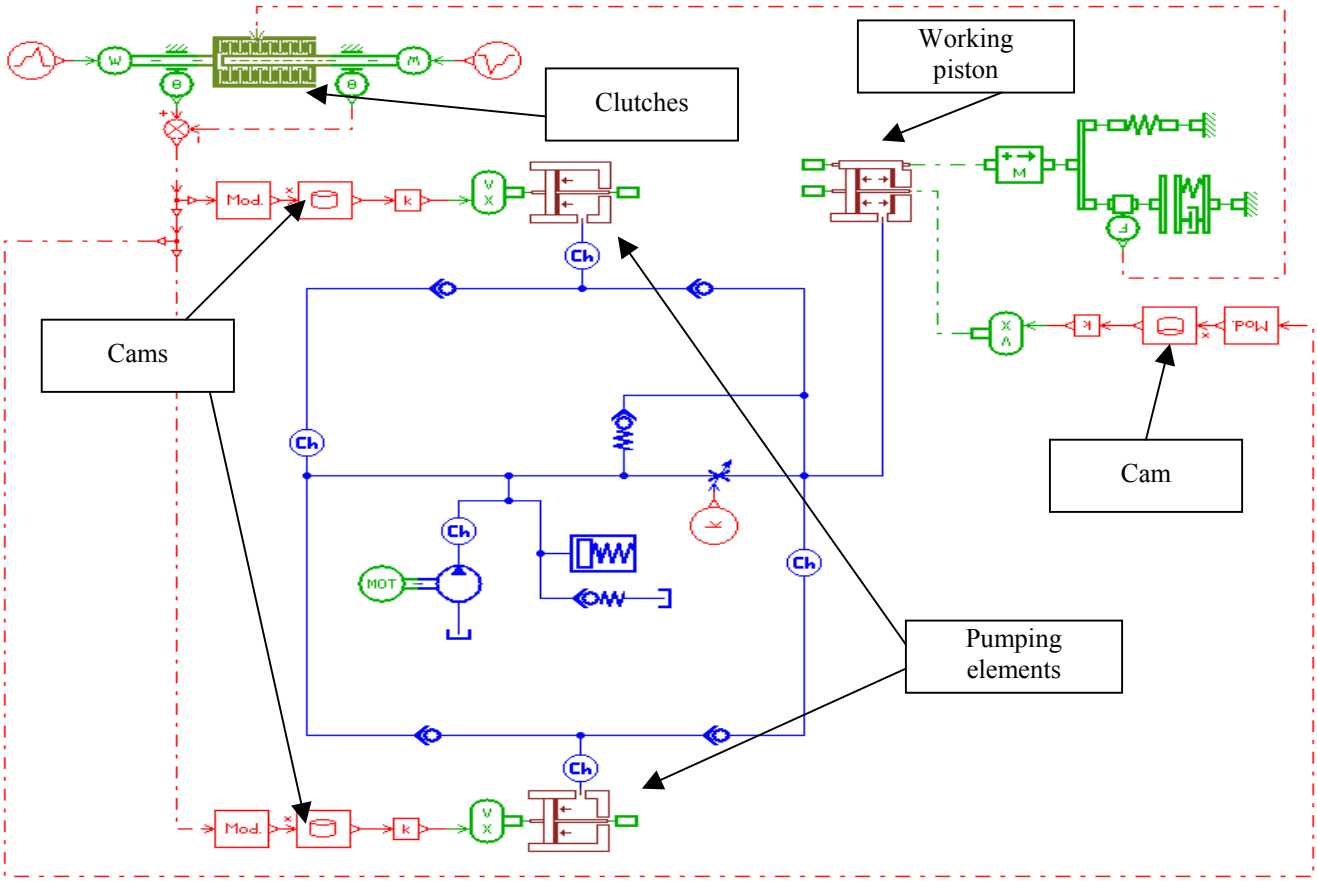

Figure 5 Sketch of the AMESim® model of the Haldex® differential

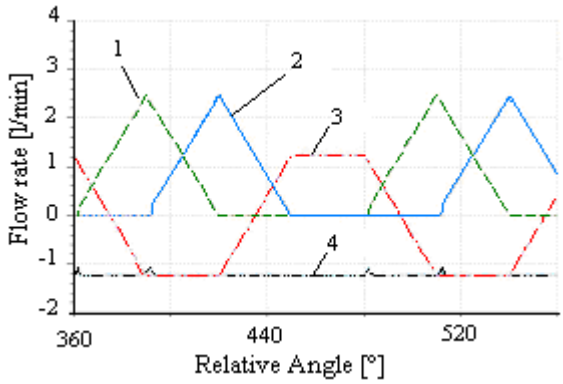

Figure 6 Oil flow rate through the three pistons of the differential and the regulation valve (simulation results)

Figure 7 plots the transmitted torque versus the relative speed of the two shafts; it is clear that Haldex® differential could work also in a stand-alone configuration, without the control algorithm, like a common LSD. Simulation permitted to obtain the actuation times, to pass from two extreme working conditions of the differential (from completely locked to completely open and vice versa), as a function of relative speed between input and output shafts. In this tests, the desired pressure was obtained by operating on the regulation valve. Actuation time appears to be very low (for example, 0.1 s) for high relative rotational speeds, like 50 rpm, and higher for low relative speeds, like 8 rpm. On the basis of simulation models, Haldex® differential appears to be optimal for on-road cars applications, due to its high flexibility in torque transmission, and not so good for off-road vehicles applications, requesting a very low reaction time also for low values of the relative speeds between the shafts.

The developed model of the differential was jointed to a Simulink® whole vehicle model, experimentally validated also for extreme dynamic manoeuvres ([2]). The whole driveline was reproduced in AMESim® (Figure 8); the gearbox permits to perform realistic manoeuvres, including changes of the gear speed ratio. Sophisticated or simplified ([1]) synchronizers models can be used according to the kind of manoeuvre. Of course, model complexity gives origin to an increase in computation time. The co-simulation models used in the activity are characterized by an average computation time which is about ten times the duration of the physical manoeuvre, with a PC with a clock frequency of 300 MHz and 128 MByte RAM.

The complex synchronizer model takes in account the geometry of all the element determining the dynamics of the system, including frictional and shape properties of the teeth. A control algorithm was developed to test the model of the physical components of Haldex® differential. The control algorithm of the differential was mainly aimed to optimise longitudinal slip distribution between the wheels, to reduce the time needed to accelerate the vehicle in extreme manoeuvres. The second target was the optimisation of the performance in extreme dynamic manoeuvres, like step steer, to reduce understeer phenomena. As a consequence, a co-simulation process was carried out between the Simulink® vehicle model, the Simulink® control strategy, and the whole driveline implemented in AMESim®.

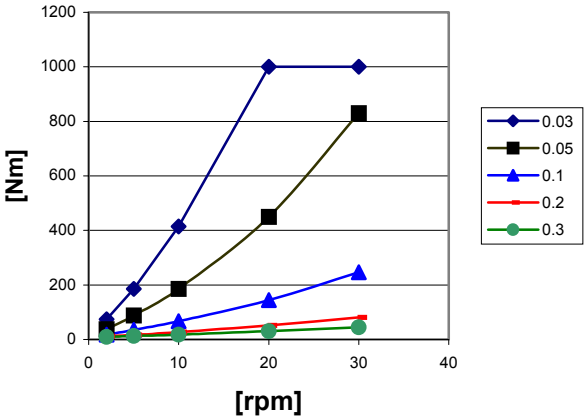

Figure 7 Example of Haldex® transmitted torque versus relative rotational speed, for different levels of regulation valve displacement (comprised between 0 and 1)

3 TORSEN® DIFFERENTIAL

The same procedure explained for Haldex® differential was applied to Torsen® differential. In this case, the analytical formulae to obtain Locking Effect mathematical expressions were written, according to the method explained in [3] for Torsen® T1. The so computed Locking Effect was used inside a Simulink® functional model of the differential. Also the model of the Torsen® T2 was built. The difference between T2 and T1 consists in the way the friction forces between the gears are generated, since in T2 all the gears are parallel and are not fixed through rods to the frame of the differential, but they are only inserted (Figure 9) in the carcass. In this paper a brief theoretical analysis of Torsen® T2 differential is presented. Figure 9 is a photograph of Torsen® T2 differential. The number of the couples of element gears can vary between 2 and 6, according to the requested specifications of the car manufacturer. The side gears ([3]) are characterized by an opposite inclination of the teeth, and are compressed one against the other while the differential is working, giving origin to a friction torque. A metal plate is inserted between the side gears to increase friction forces. The first step to obtain locking effect formula consists in writing the kinematical equations for the coupled gearwheels. According to the scheme of Figure 10, it is possible to write the following equations:

$$V1 = \omega_1 \cdot R_2 \tag{1}$$

$$V2 = \omega_m \cdot R_2 \tag{2}$$

$$Vm = \omega_m \cdot (R_1 + R_2) \tag{3}$$

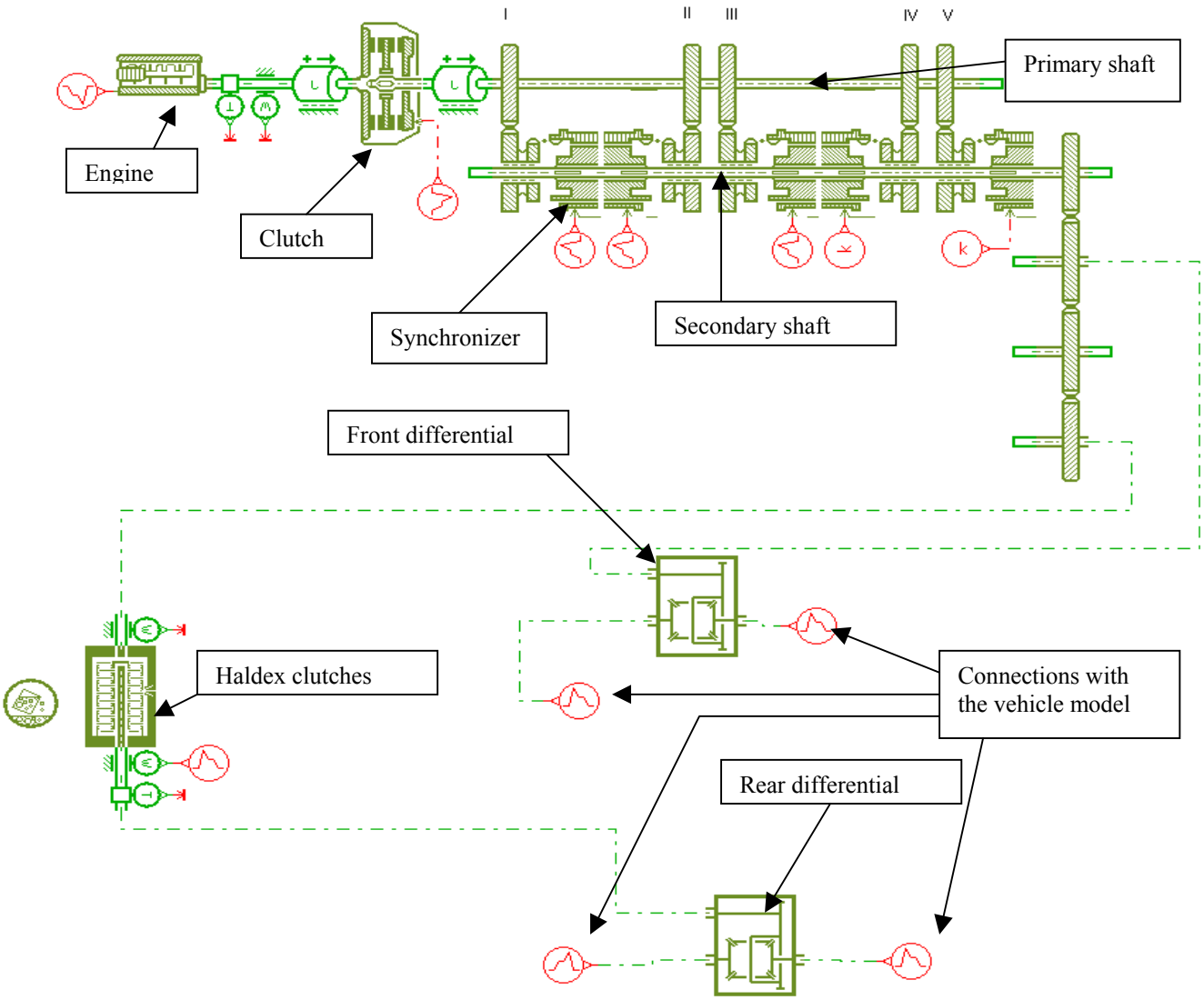

Figure 8 Example of model of the whole driveline used for co-simulation with the vehicle model

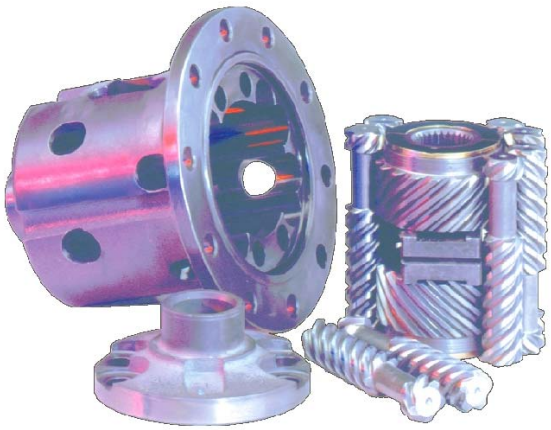

Figure 9 Torsen® T2 differential

where ω_1 is left side gear rotational speed, ω_2 is left side gear rotational speed, R_2 is side gear radius, ω_m is frame angular speed, R_1 is the element gear radius. Frame angular speed ω_m for a differential is:

$$\omega_m = \frac{\omega_1 + \omega_2}{2} \tag{4}$$

Since side gear and element gear are coupled, their peripheral velocities have to be the same:

$$V1 = V2 \tag{5}$$

$$\omega_1 \cdot R_2 = \omega_m \cdot R_2 \tag{6}$$

If ω_1 is different from ω_2, the element gear will start to rotate around its axis according to the following equation, corresponding to the velocity arrays of Figure 11:

$$\omega_1 \cdot R_2 = \omega_m \cdot R_2 - \omega_b \cdot R_1 \tag{7}$$

that is:

$$\omega_b = \left(\frac{\omega_2 - \omega_1}{2} \right) \cdot \frac{R_2}{R_1} \tag{8}$$

where ω_b is the element gear rotational speed around its own axis. The same procedure has to be followed for the right side gear. The following step consists in writing the equations of the forces and torques acting on the different components, along the directions X, Y and Z (Figure 12).

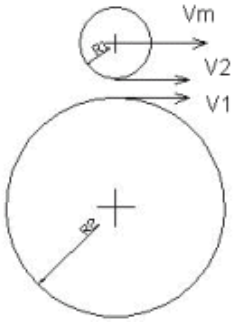

Figure 10 Kinematical scheme of the left side gear (radius R_2) with its element gear (radius R_1)

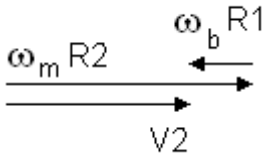

Figure 11 Velocity vectors in the kinematical coupling of the left side gear

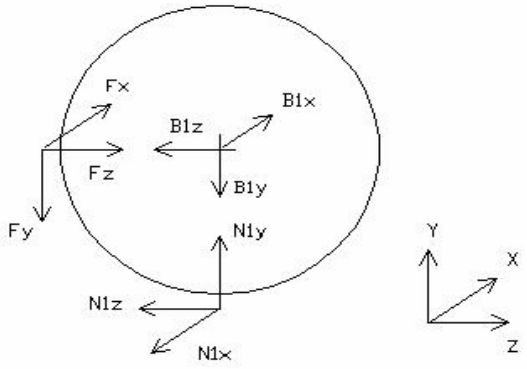

Figure 12 Force components acting on the right element gear

The following formulae are about the right element gear (Figure 12):

$$\sum F_x = 0 \tag{9}$$

$$B_{1x} + F_x - N_{1x} + F_{1f} \cdot \cos\vartheta = 0 \tag{10}$$

$$\sum F_y = 0 \tag{11}$$

$$-B_{1y} - F_y + N_{1y} = 0 \tag{12}$$

$$\sum F_z = 0 \tag{13}$$

$$-B_{1z} - N_{1z} - F_{1f} \sin\vartheta + F_z = 0 \tag{14}$$

$$\sum M_x = 0 \tag{15}$$

$$-F_y R_1 + N_{1z} R_1 + F_{1f} R_1 \sin\vartheta - \mu_b (B_{1z} + B_{1y}) R_{bs} - \mu_b B_{1x} R_s = 0 \tag{16}$$

where $N_{1x,y,z}$ are the forces between the element gear and the side gear, $B_{1x,y,z}$ are the vinculum forces of the frame, $F_{x,y,z}$ (in (10), (12), (14) and (16)) are the forces between the two element gears, F_{1f} is friction force on the helical teeth, θ is the helix angle, μ_b is friction coefficient between the element gear and the frame, R_{bs} is the external radius of the teeth, R_s is the application radius of the friction force on the plane perpendicular to X-axis.

The same process has to be applied to the left side gear (Figure 13):

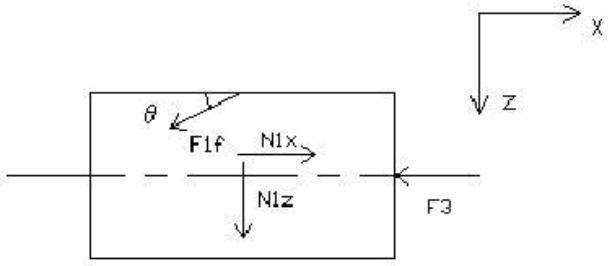

Figure 13 Forces acting on the left side gear in the plane XZ

$$\sum F_x = 0 \tag{17}$$

$$N_{1x} - F_{1f} \cdot \cos\vartheta - F_3 = 0 \tag{18}$$

$$\sum M_x = 0 \tag{19}$$

$$R_3 (N_{1z} + F_{1f} \sin\theta) + R_c \mu_3 F_3 = T_1 \tag{20}$$

where T_1 is the torque acting on the output shaft, R_3 is the radius of the left side gear, R_c is the application radius of the friction force on the plane perpendicular to x-axis, μ_3 is the friction coefficient between the side gear and the metal plate. For simplicity, (17)-(20) considered only one element gear; when considering 4 element gears, they become:

$$\sum F_x = 0 \tag{21}$$

$$4N_{1x} - 4F_{1f} \cdot \cos\vartheta - F_3 = 0 \tag{22}$$

$$\sum M_x = 0 \tag{23}$$

$$4 \cdot R_3 (N_{1z} + F_{1f} \sin\theta) + R_c \mu_3 F_3 = T_1 \tag{24}$$

Similar formulae can be applied to the left element gear and the right side gear. It is necessary to write the equations stating the relationships between the forces according to the geometry of the gear wheels. For example, Figure 14 is about the coupling between the side gear and the element gear; θ and φ are the helix angle and the pressure angle of the gears.

$$N_{1x} = N_{1z} \tan\vartheta \tag{25}$$

$$N_{1y} = N_{1z} \tan\phi/\cos\vartheta \tag{26}$$

$$N_{2x} = N_{2z} \tan\vartheta \tag{27}$$

$$N_{2y} = N_{2z} \tan\phi/\cos\vartheta \tag{28}$$

where $N_{2x,y,z}$ are the forces between the element gear and the side gear.

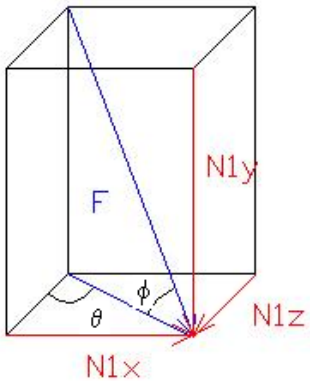

Figure 14 Forces between side gear and element gear; components along X and Y as a function of the component along Z

It is possible, through the scheme of Figure 14, to write friction forces between the teeth of the gearwheels, as the product of the friction coefficient and the normal forces acting on the teeth.

$$F_{1f} = \mu_1 N_{1z}/(\cos\vartheta\cos\phi) \tag{29}$$

The same equation can be obtained for the other side of the differential. By putting together all the presented equations, it is possible to obtain the expression of the Torque Bias Ratio (TBR or simply BR, [3], [4]) for the Torsen® T2 differential:

$$\frac{T_1}{T_2} = \frac{N_{1z}A}{N_{2z}B} \tag{30}$$

where:

$$A = R_3 + R_3\mu_1 \tan\vartheta/\cos\phi + R_c\mu_3(\tan\vartheta - \mu_1/\cos\phi) \tag{31}$$

$$B = R_3 - R_3\mu_2 \tan\vartheta/\cos\phi - R_c\mu_4(\tan\vartheta + \mu_2/\cos\phi) \tag{32}$$

$$N_{1z}/N_{2z} = (S_1S_3)/(S_2S_4) \tag{33}$$

$$S_1 = R_1\left(1 - \frac{\mu_2\tan\vartheta}{\cos\phi}\right) + \mu_s R_s\left(\tan\vartheta + \frac{\mu_2}{\cos\phi}\right) + \mu_b R_{bs}\left(1 + \frac{\tan\phi}{\cos\vartheta} - \frac{\mu_2\tan\vartheta}{\cos\phi}\right) \tag{34}$$

$$S_2 = R_1\frac{\tan\phi}{\cos\vartheta} - \mu_b R_{bs}\left(1 + \frac{\tan\phi}{\cos\vartheta}\right) + \mu_s R_s\tan\vartheta \tag{35}$$

$$S_3 = R_1\frac{\tan\phi}{\cos\vartheta} - \mu_b R_{bs}\left(\frac{\tan\phi}{\cos\vartheta} - 1\right) - \mu_s R_s\tan\vartheta \tag{36}$$

$$S_4 = R_1 + \mu_1\frac{\tan\vartheta}{\cos\phi} - \mu_s R_s\left(\tan\vartheta + \frac{\mu_1}{\cos\phi}\right) + \mu_b R_{bs}\left(1 + \frac{\mu_1\tan\vartheta}{\cos\phi} - \frac{\tan\phi}{\cos\vartheta}\right) \tag{37}$$

By applying these formulae, it is possible to express TBR as a function of one of the several design parameters, for example the helix angle of the gears (Figure 15). Curves 1 and 2 are computed for different friction coefficients between the side gears and the central metal plate; they can be modified on the real differential by inserting devoted friction discs.

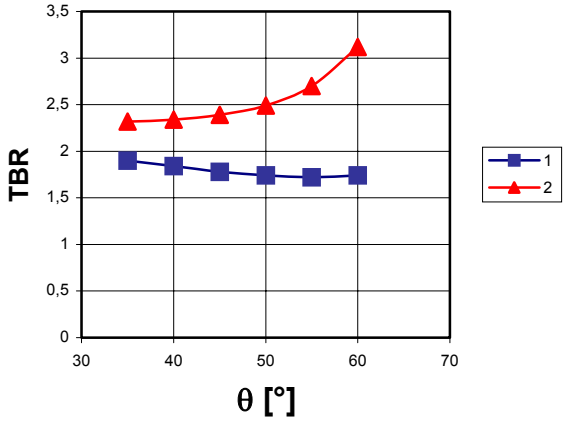

Figure 15 Torque Bias Ratio as a function of the helix angle; 1: friction coefficient between the side gears and the metal plate = 0.0025, 2: friction coefficient between the side gears and the metal plate = 0.15

Also the power lost in the differential was computed by considering all the terms, due to friction phenomena on the gear wheels, friction between the side gears and the central metal plate, friction between the element gears and the frame. The obtained Torque Bias Ratio (BR) was inserted inside a Simulink® functional model ([4]) of Torsen differential, having as main input the Locking Effect, defined by the following equation:

$$LE = \frac{T_1 - T_2}{T_1 + T_2} \tag{38}$$

LE can be expressed as a function of BR:

$$LE = \frac{BR - 1}{BR + 1} \tag{39}$$

In a typical application, Torsen® differential can be used as a central differential; in this case the Simulink® model computes the angular speed Ω of the frame of the differential [4]:

$$\Omega = \frac{\omega_{front} + SR \cdot \omega_{rear}}{1 + SR} \tag{40}$$

where ω_{front} is front differential frame angular speed, ω_{rear} is rear differential frame angular speed, SR is the Split Ratio, defined as the torque distribution between the two axles. SR is defined by the ratio of the two side gears of Torsen® differential. SR is 1:1 in most applications.

According to the model, Torsen® differential can work in three different conditions:

- open if the angular speed of the axles is the same; in this case, the torques are the same on the two axles;
- if the angular speeds are not the same (and they are characterized by a consistent difference), the torque distribution is computed according to LE;
- in a condition intermediate between the other two; in this condition the transferred torques or the relative speeds are not so high to determine element gears rotation around their axis. The differential is locked; it acts like a torsion spring, with a stiffness depending on the gear wheels.

The model identifies, instant by instant, the operating condition of the differential and then computes the torques for the two axles.

4 GKN PWR TRAK® DIFFERENTIAL

The same mathematical procedure was repeated for the GKN PWR TRAK® differential (Figure 16). It is another example of torque sensing differential, with a different configuration of the gears.

Figure 16 GKN PWR TRAK® differential

In this case, the element gears are not equal each other, in each couple; one is longer than the other (Figure 17). Between the two side gears, a metal block is located to increase friction. Also for this application a parametric study about the influence of each design parameter was carried out. For example, Figure 18 shows TBR versus the helix angle of the gears, for different conditions of friction between the internal components of the differential. The same Simulink® model adopted for Torsen® differential was used for simulating GKN PWR TRAK®.

Figure 17 The gears of the GKN PWR TRAK® differential

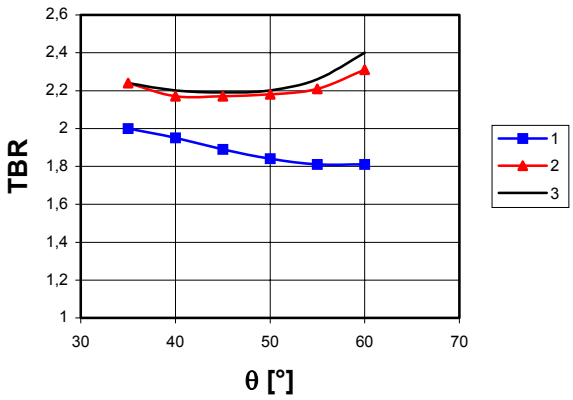

Figure 18 TBR versus helix angle for a GKN PWR TRAK® differential; 1: no friction between the side gears and the central element (metal block) and side gears and frame; 2: friction between the side gears and the metal block; 3: friction between the side gears and the metal block and between the side gears and the frame

5 GKN VISCODRIVE® DIFFERENTIAL

Figure 19 is a photograph of a GKN Visco-Drive® differential ([5]), usually adopted to distribute the torque between the front and the rear axle. The metal discs inside the differential have a consistent backlash between themselves, since they do not have to get in contact each other. The torque is transmitted by the viscous properties of a devoted fluid. This differential can be modelled with the classical equations of viscous momentum:

$$M_v = \int_A r\tau \cdot dA \tag{41}$$

$$\tau = \mu \frac{U}{h} = \mu \frac{\omega \cdot r}{h} \tag{42}$$

$$M_v = \int_{R_i}^{R_e} \mu \frac{\omega \cdot r}{h} \cdot 2\pi \cdot r^2 dr \tag{43}$$

$$M_v = 2\pi \frac{\mu\omega}{h}\left(\frac{R_e^4}{4} - \frac{R_i^4}{4}\right) \tag{44}$$

where M_v is the viscous moment, r is a generic radius, τ is the shear stress, A is the area of a disc, U is the linear relative speed of a point of a disc at the radius r, ω is relative rotational speed, h is the distance between the discs, μ is the dynamic viscosity of the fluid, R_e and R_i (for example, 5.25 cm and 3.25 cm, for the differential considered in this research work) are the external and internal radii of a disc.

Figure 19 GKN Visco-Drive® differential

By considering the total number N of the active surfaces and the area correction factor ξ, the total viscous moment of the differential is:

$$M_v = 2\pi \cdot N\xi \frac{\mu\omega}{h}\left(\frac{R_e^4}{4} - \frac{R_i^4}{4}\right) \tag{45}$$

ξ takes in account the real shape of the discs and was estimated equal to 0.9 in the case of the considered differential, equipped with 26 discs linked to the input shaft and 25 discs linked to the output shaft. The following momentum equations complete the model of the differential:

$$C_r - M_v - I_c\dot{\omega}_c = 0 \tag{46}$$

$$C_p - M_v + I_p\dot{\omega}_p = 0 \tag{47}$$

where C_r is the torque acting on the transmission shaft, C_p is the torque to the rear differential, I_c is the inertial momentum of the external discs and the frame (with an angular velocity ω_c), I_p is the inertial momentum of the internal discs and the output shaft, having an angular velocity ω_p.

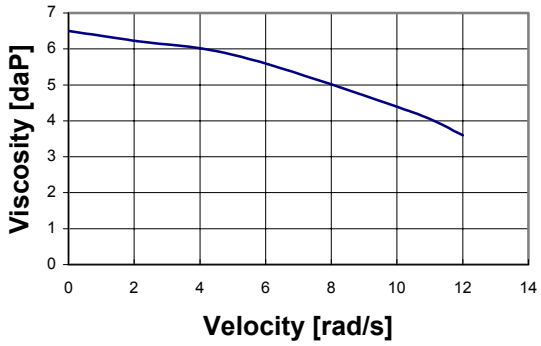

Figure 20 Viscosity versus angular velocity characteristic (typical qualitative behaviour)

To obtain realistic results, the model has to take in account the dependency of the fluid viscosity on the angular speed. A typical curve is contained in Figure 20; this characteristic depends on the temperature of the differential. In the model different characteristics corresponding to several temperatures were inserted; the simulations were performed at fixed values of temperature or at imposed temperature variations. The next step in the development of the model will consist in building a thermal model of the differential, to simulate the real variation of the temperature.
For fixed values of temperature, the model gave origin to results, which were experimentally validated (Figure 21) through tests performed at Politecnico di Torino differentials test bench ([2]). Also the Visco-Drive® model was inserted in a vehicle model.

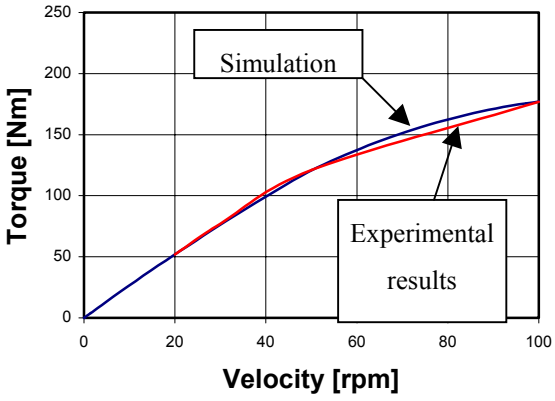

Figure 21 Comparison between simulation and experimental results

An evolution of the Visco-Drive® is represented by Visco-Lock®, which is characterized, in addition to the tangential viscous effect in correspondence of relative velocity, by a normal force compressing the discs, due to a pumping element which is activated by the relative rotational speed. In such a way, the differential can increase the torque transmitted to the rear axle, in spite of the same external

size (the dimensions of the pumping element can be neglected).

6 COMPARISON BETWEEN THE DIFFERENT DRIVELINE LAYOUTS

The models of different AWD layouts were compared in a wide variety of extreme dynamic manoeuvres, to evaluate the peculiarities of each solution. This is the same method followed by [6] for the case of 2WD vehicles.

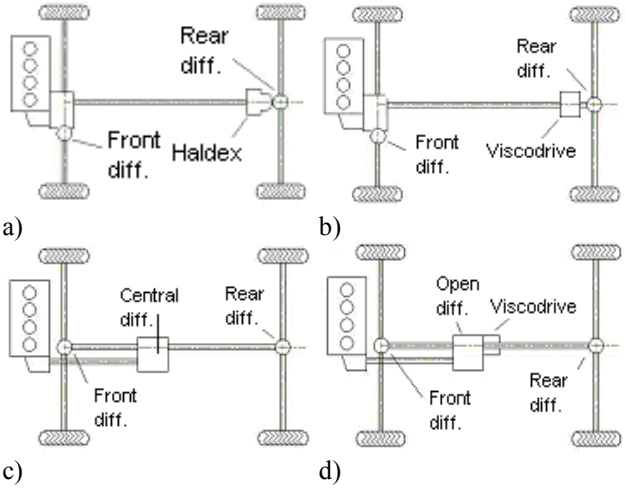

Figure 22 Schemes of some of the different configurations of driveline layouts tested by the presented models

Figure 22 presents the layouts of the different solutions: a) is the scheme of the transmission including Haldex® differential in the central location, b) is the scheme of the transmission including Visco-Drive® in the central location, c) is the scheme of the transmission including an Open differential or a Torsen® differential (TBR = 3) in central location, d) is the scheme of the transmission including an Open differential together with a Visco-Drive® in central location. In the vehicle model, mass and inertial properties variation due to the different layouts was taken in consideration. The data inserted in the vehicle model belong to a middle class sedan, characterized by a front engine and a front wheel driven configuration in the 2WD version. Active systems, like Anti-Slip Regulator (ASR) or Electronic Stability program (ESP), were not considered. Of course, the results of the comparisons presented in Figures 23-30 have to be considered indicative of the potential of simulation analysis, and not an absolute index of evaluation of each driveline layout. In fact, it is sufficient to change some of the tuning parameters of each configuration to obtain consistently different performances. As a consequence, the process of modifying and testing that automotive manufacturers use to evaluate different solutions can be performed at the level of PC simulation, and not on the road, at least during the first steps of the design process. Figure 23 is about a simulated acceleration test in high adherence conditions; it plots vehicle longitudinal speed at the end of the manoeuvre, characterized by the same duration for all the driveline layouts. It is evident the increased performance related to 4WD layouts compared to the Front Wheel Drive layout and the Rear Wheel Drive layout.

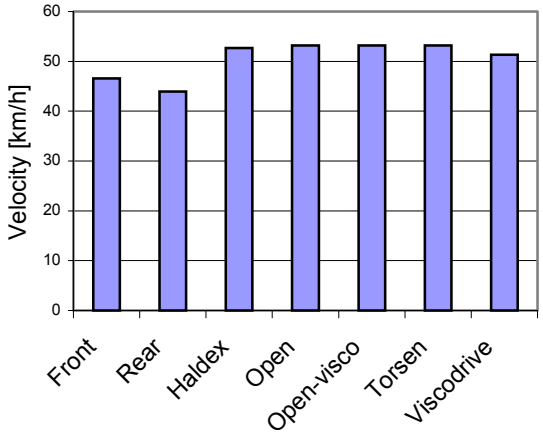

Figure 23 Acceleration test in high adherence conditions; longitudinal speed values at the end of the manoeuvres for different driveline layouts

The same test, performed in low adherence conditions (Figure 24), does not put in evidence consistent differences between the AWD layouts, characterized by a better performance than the 2WD vehicles. Especially in high adherence conditions, Torsen® differential seems to guarantee a more uniform distribution of tires longitudinal slips between the two axles, due to the very small delays in actuation also for low values of the relative speed between the two axles. Of course, this advantage of Torsen® over Haldex® and Visco-Drive® differentials is more evident in high adherence conditions, when the relative speed between the two axles is limited.

The same manoeuvre in split-μ conditions (with a different friction coefficient between tires and ground on the two sides of the vehicle, Figure 25) gave origin to critical results for the rear wheel driven vehicle, not only in terms of longitudinal velocity, but also of body yaw acceleration. It was necessary to simulate engine dynamics in an accurate way to obtain realistic results in split-μ conditions. In particular, it was emulated the behaviour of the engine speed limiter, giving origin to an important torque reduction when the engine reaches its maximum rotational velocity. If engine speed limiter were not considered, the low friction wheel would continue to accelerate during the manoeuvre. Its inertial torque would permit the development of a consistent traction force on the driven wheels in high adherence. This phenomenon would continue during the whole manoeuvre. By considering engine speed limiter, the correct dynamics was taken in account in split-μ conditions. When the low adherence wheel starts to accelerate due to the excessive engine torque, the high adherence wheel of the same axle can absorb the engine torque corresponding to its friction level.

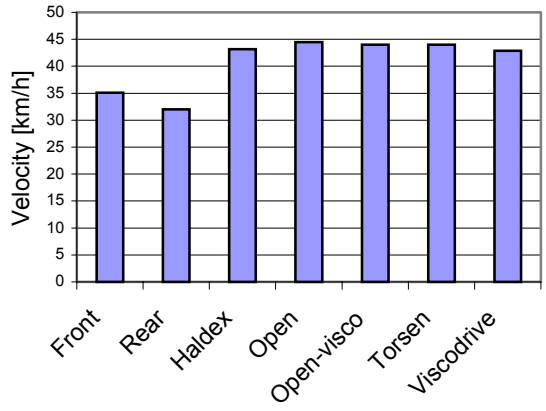

Figure 24 Results for the same test of Figure 23, in low adherence conditions

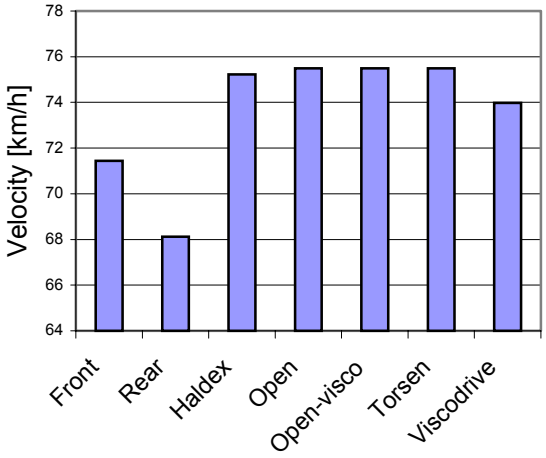

Figure 25 Acceleration test in split-μ conditions; longitudinal speed values at the end of the manoeuvres for different driveline layouts

Only when the engine reaches its maximum rotational speed, engine speed limiter intervenes to maintain engine speed at that fixed level, by reducing engine torque. Inertial torque on the low adherence wheel disappears, giving origin to a corresponding reduction of the torque of the wheel in high adherence conditions. From that instant the low and high adherence wheels transmit the same traction force, corresponding to that of the low adherence wheel. The advantage is that the generation of consistent body yaw rate accelerations is prevented. The inconvenience is that it cannot be reached the maximum level of longitudinal acceleration. This kind of limitation can be solved by the adoption of self-locking differentials not only to distribute engine torque between the axles, but also within the same axle. The same split-μ test was repeated (Figures 26 and 27) for 2WD vehicles equipped with GKN POWR-TRAK® differentials (TBR = 2.07) on the driven axle. GKN front differential has the best performance from the point of view of longitudinal speed; also yaw acceleration should be controllable for a skilled driver.

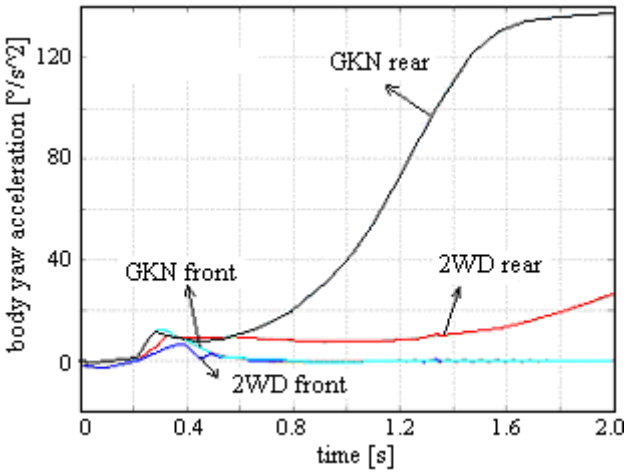

Figure 26 Acceleration test in split-μ conditions; body yaw acceleration versus time

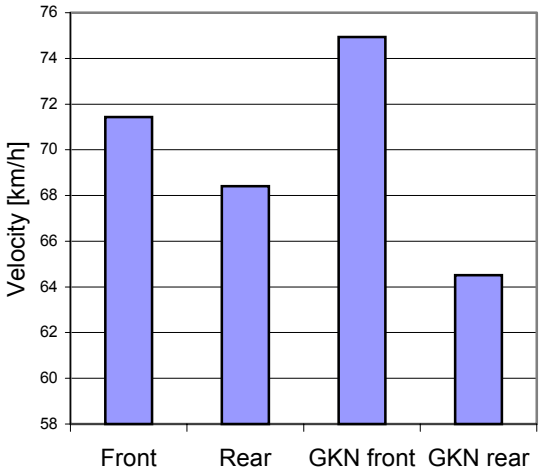

Figure 27 Acceleration test in split-μ conditions; longitudinal speed values at the end of the manoeuvres for different driveline layouts (2WD vehicles)

GKN differential on the rear axle determines an excessive level of body yaw acceleration, provoking a dangerous oversteer. At the moment, car manufacturers prefer to obtain the same results without using a self-locking differential on the driven axle, but by adopting an ESP (Electronic Stability Program) unit acting on brakes and engine control. ESP permits a smoother level of control both on longitudinal acceleration and yaw acceleration if compared to a mechanical LSD or a torque sensitive differential. The inconvenience of ESP intervention on brakes is that it has to be limited, not to have reliability problems of the components of the driveline. As a consequence of all these considerations, in most applications self-locking differentials are used to distribute the torque between the axles and are mounted in the central location.

Figures 28-30 are a comparison of the different driveline layouts from the point of view of lateral dynamics, during a

single and a double step steer in wide open throttle conditions and with gas released, to excite oversteer. In this kind of manoeuvres, it is fundamental to limit body sideslip angle values, not to have an uncontrollable vehicle.

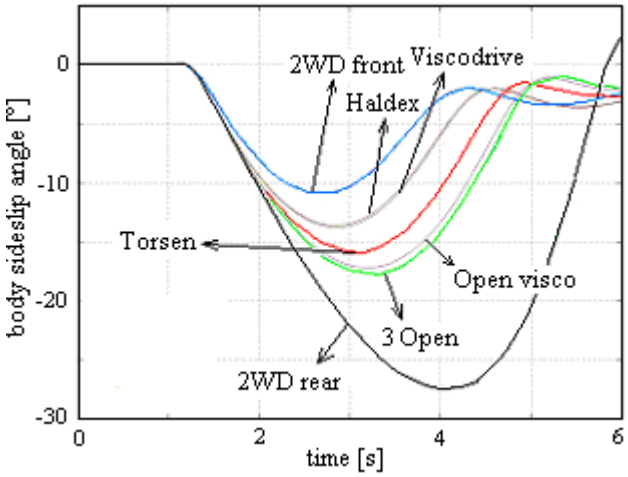

Figure 28 Extreme step steer manoeuvre with gas released; body sideslip angle versus time for different driveline layouts

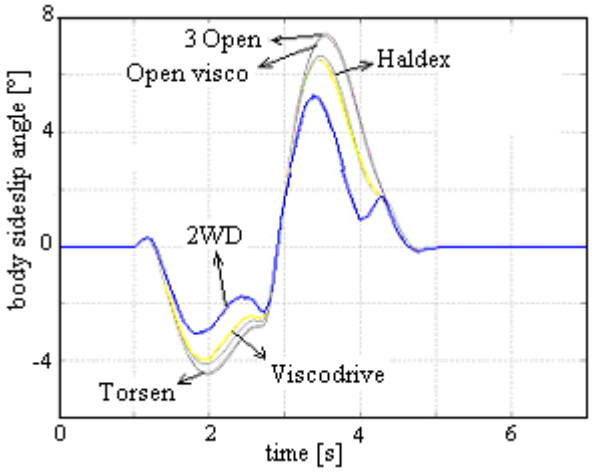

Figure 29 Extreme double step steer manoeuvre with wide open throttle; body sideslip angle versus time for different driveline layouts

Figure 30 shows the minimum and the maximum value of body sideslip angle during the double step steer for the different driveline layouts. The front wheel driven car seems to be the most stable, immediately followed by the AWD equipped with the Haldex® differential, having a control algorithm capable of taking in account also lateral dynamics. Passive central differentials give origin to a less safe behaviour, since they tend to transfer torque to the rear axle as a consequence of front/rear relative longitudinal slip, independently of lateral dynamics. In conclusion, Torsen®, used as a central differential, seems to be the best solution to solve traction problems, whereas Haldex® seems to be the best compromise between longitudinal and lateral dynamics.

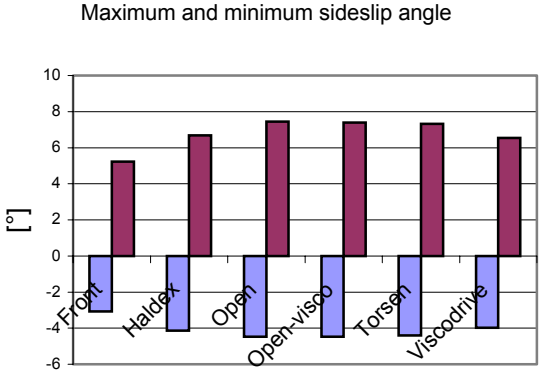

Figure 30 Extreme double step steer manoeuvre with wide open throttle: maximum and minimum body sideslip angle values for different driveline layouts

7 CONCLUSIONS

Simulation appears to be a useful instrument to evaluate the performance of different All-Wheels-Drive systems layouts in terms of vehicle dynamics. The models presented in the paper, especially those related to Haldex® differential and Torsen® differential, should permit the definition of the design criteria of these components. In fact, they allow the evaluation of the internal behaviour of the component and its variation due to the modification of its parameters.

REFERENCES

[1] Garcia O. and Kargar K., Simulation tool for transmission and driveline systems design. *SAE Technical Paper*, 2000-01-0832, 2000.

[2] Danesin D., Krief P., Suraci E., Velardocchia M. and Brusa E., Modelling vehicle dynamics for virtual experimentation, road tests supporting and dynamic control. *SAE Technical Paper*, 2002-01-0815, 2002.

[3] Shih S. and Bowermann W., An evaluation of torque bias and efficiency of Torsen differential. *SAE Technical Paper*, 2002-01-1046, 2002.

[4] Morgando A., Sorniotti A., Velardocchia M., Danesin D. and Girardin C., Influence of driveline design parameters on vehicle behaviour. *SAE Technical Paper*, 2004-01-0860, 2004.

[5] Gassmann T. and Barlage J., VISCO-LOCK: a speed sensing limited-slip device with high torque progressive engagement. *SAE Technical Paper*, 970684, 1997.

[6] Huchtkoetter H. and Klein H., The effect of various limited-slip differentials in front wheel drive vehicles on handling and traction. *SAE Technical Paper*, 960717, 1996.

ISSN 1590-8844
International Journal of Mechanics and Control, Vol. 06, No. 01, 2005

TEMPLATE FOR PREPARING PAPERS FOR PUBLISHING IN INTERNATIONAL JOURNAL OF MECHANICS AND CONTROL

Author1* Author2**

* affiliation Author1

** affiliation Author2

ABSTRACT

This is a brief guide to prepare papers in a better style for publishing in International Journal of Mechanics and Control (JoMaC). It gives details of the preferred style in a template format to ease paper presentation. The abstract must be able to indicate the principal authors' contribution to the argument containing the chosen method and the obtained results.

Keywords: keywords list (max 5 words)

1 TITLE OF SECTION (E.G. INTRODUCTION)

This sample article is to show you how to prepare papers in a standard style for publishing in International Journal of Mechanics and Control.
It offers you a template for paper layout, and describes points you should notice before you submit your papers.

2 PREPARATION OF PAPERS

2.1 SUBMISSION OF PAPERS

The papers should be submitted in the form of an electronic document, either in Microsoft Word format (Word'97 version or earlier).
In addition to the electronic version a hardcopy of the complete paper including diagrams with annotations must be supplied. The final format of the papers will be A4 page size with a two column layout. The text will be Times New Roman font size 10.

Contact author: author1[1], author2[2]

[1]Address of author1.

[2]Address of author2 if different from author1's address.

2.2 DETAILS OF PAPER LAYOUT

2.2.1 Style of Writing

The language is English and with UK/European spelling. The papers should be written in the third person. Related work conducted elsewhere may be criticised but not the individuals conducting the work. The paper should be comprehensible both to specialists in the appropriate field and to those with a general understanding of the subject.
Company names or advertising, direct or indirect, is not permitted and product names will only be included at the discretion of the editor. Abbreviations should be spelt out in full the first time they appear and their abbreviated form included in brackets immediately after. Words used in a special context should appear in inverted single quotation mark the first time they appear. Papers are accepted also on the basis that they may be edited for style and language.

2.2.2 Paper length

Paper length is free, but should normally not exceed 10000 words and twenty illustrations.

2.2.3 Diagrams and figures

Figures and Tables will either be entered in one column or two columns and should be 80 mm or 160 mm wide respectively. A minimum line width of 1 point is required at actual size. Captions and annotations should be in 10 point with the first letter only capitalised *at actual size* (see Figure 1 and Table VII).

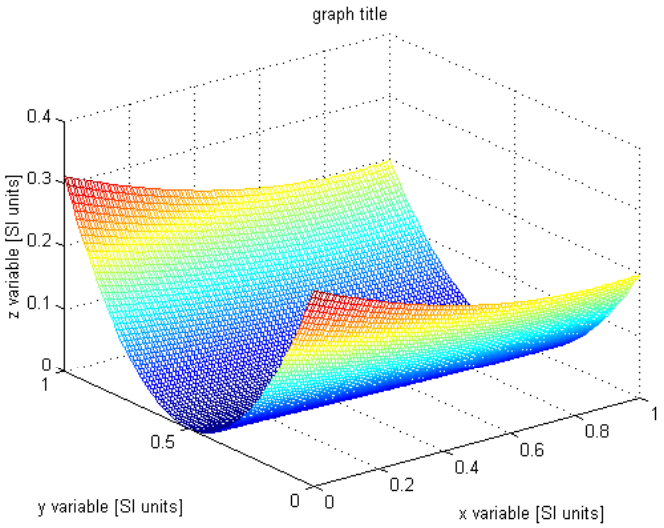

Table VII - Experimental values

Robot Arm Velocity (rad/s)	Motor Torque (Nm)
0.123	10.123
1.456	20.234
2.789	30.345
3.012	40.456

2.2.4 Photographs and illustrations
Authors could wish to publish in full colour photographs and illustrations. Photographs and illustrations should be included in the electronic document and a copy of their original sent. Illustrations in full colour ….

2.2.5. Equations
Each equation should occur on a new line with uniform spacing from adjacent text as indicated in this template. The equations, where they are referred to in the text, should be numbered sequentially and their identifier enclosed in parenthesis, right justified. The symbols, where referred to in the text, should be italicised.

- point 1
  - point 2
    - point 3

1. numbered point 1
   2. numbered point 2
      3. numbered point 3

$$\vec{F} = m\,\vec{a} \qquad (1)$$

3 COPYRIGHT

Authors will be asked to sign a copyright transfer form prior to JoMaC publishing of their paper. Reproduction of any part of the publication is not allowed elsewhere without permission from JoMaC whose prior publication must be cited. The understanding is that they have been neither previously published nor submitted concurrently to any other publisher.

4 PEER REVIEW

Papers for publication in JoMaC will first undergo review by anonymous, impartial specialists in the appropriate field. Based on the comments of the referees the Editor will decide on acceptance, revision or rejection. The authors will be provided with copies of the reviewers' remarks to aid in revision and improvement where appropriate.

5 REFERENCES (DESCRIPTION)

The papers in the reference list must be cited in the text. In the text the citation should appear in square brackets [ ], as in, for example, "the red fox has been shown to jump the black cat [3] but not when...". In the Reference list the font should be Times New Roman with 10 point size. Author's first names should be terminated by a 'full stop'. The reference number should be enclosed in brackets.
The book titles should be in *italics*, followed by a 'full stop'. Proceedings or journal titles should be in *italics.* For instance:

REFERENCES (EXAMPLE)

[1] Smith J., Jones B. and Brown J., *Title of the book*. 1st edition, Publisher, 2001.

[2] Smith J., Jones B. and Brown J., Title of the paper. *Proc. of Conference Name*, where it took place, Vol. 1, paper number, pp. 1-11, 2001.

[3] Smith J., Jones B. and Brown J., Title of the paper. *Journal Name*, Vol. 1, No. 1, pp. 1-11, 2001.

[4] Smith J., Jones B. and Brown J., *Patent title*, U.S. Patent number, Nov. 4, 2001.

International Journal of Mechanics and Control – JoMaC
Published by Levrotto&Bella
TRANSFER OF COPYRIGHT AGREEMENT

NOTE: Authors/copyright holders are asked to complete this form signing section A, B or C and mail it to the editor office with the manuscript or as soon afterwards as possible.	*Editor's office address:* Andrea Manuello Bertetto Elvio Bonisoli *Dept. of Mechanics* *Technical University-Politecnico di Torino* ***C.so Duca degli Abruzzi, 24. 10129 Torino – Italy*** e_mail: jomac@polito.it fax n.: +39.011.564.6999

The article title:

By:_____

To be Published in ***International Journal of Mechanics and Control JoMaC***
Official legal Turin court registration Number 5320 (5 May 2000) - reg. Tribunale di Torino N. 5390 del 5 maggio 2000

A Copyright to the above article is hereby transferred to the JoMaC, effective upon acceptance for publication. However the following rights are reserved by the author(s)/copyright holder(s):
1. All proprietary rights other than copyright, such as patent rights;
2. The right to use, free or charge, all or part of this article in future works of their own, such as books and lectures;
3. The right to reproduce the article for their own purposes provided the copies are not offered for sale.

To be signed below by all authors or, if signed by only one author on behalf of all co-authors, the statement A2 below must be signed.

A1. All authors:

SIGNATURE_____DATE_____ SIGNATURE_____DATE_____

PRINTED NAME_____ PRINTED NAME_____

SIGNATURE_____DATE_____ SIGNATURE_____DATE_____

PRINTED NAME_____ PRINTED NAME_____

A2. One author on behalf of all co-authors:
"I represent and warrant that I am authorised to execute this transfer of copyright on behalf of all the authors of the article referred to above"

PRINTED NAME_____

SIGNATURE_____ TITLE_____ DATE_____

B. The above article was written as part of duties as an employee or otherwise as a work made for hire. As an authorised representative of the employer or other proprietor. I hereby transfer copyright to the above article to Editel-Pozzo Gros Monti effective upon publication. However, the following rights are reserved:
1. All proprietary rights other than copyright, such as patent rights;
2. The right to use, free or charge, all or part of this article in future works of their own, such as books and lectures;
3. The right to reproduce the article for their own purposes provided the copies are not offered for sale.

PRINTED NAME_____

SIGNATURE_____ TITLE_____ DATE_____

C. I certify that the above article has been written in the course of employment by the United States Government so that no copyright exists, or by the United Kingdom Government (Crown Copyright), thus there is no transfer of copyright.

PRINTED NAME_____

SIGNATURE_____ TITLE_____ DATE_____

CONTENTS

next number scheduled titles:

Data Fusion From CCD Camera and Ultrasound Scanning Locator
D. Janglová, I. Kello, I. Považ an, L. Uher, S. Vagner

2D and 3D Numerical Analysis of Flow in a Bi-directional Cavo-Pulmonary Anastomosis
C. Delprete and R. Sesana

A 14 D.O.F. Model for fhe Evaluation ff Vehicle's Dynamics: Numerical-Experimental Comparison
F. Cheli, E. Leo, S. Melzi and F. Mancosu

Fractal Rules of Mixture for Multi-Scale Fragmentation of Heterogeneous Materials
A. Carpinteri and N. Pugno

MEMS Inertial Guidance Systems for Low Cost Vehicles
P. Maggiore and M. Velardocchia